UNIVERSITY OF TARTU

Faculty of Science and Technology

Institute of Chemistry

Egert Möller

Electrospinning and Subsequent Pyrolysis of $ZnCl_2$-doped Polyacrylonitrile Mats for the Synthesis of Activated Carbon Nanofibers

Master's Thesis (30 ECTs)

Materials Science and Technology

Supervisors: Rasmus Palm, Ph. D

Tartu 2023

$ZnCl_2$-ga dopeeritud polüakrülonitriilist elektroformeeritud kiudmattide pürolüüs aktiveeritud süsiniknanokiude sünteesiks

Kliimaeesmärkide ning taastuvenergeetika arengu valguses on tekkinud suurenenud nõudlus mitmete uudsete spetsiifiliste omadustega materjalide järele. Erilist tähelepanu pööratakse nanokiudmaterjalidele, millel on energeetika- ja laiemalt ka tööstusvaldkonnas palju erinevaid rakendusi.

Esimese etapina elektroformeeriti kuus polüakrülonitriilist $ZnCl_2$-ga dopeeritud kiudmatti. Valmistatud polümeermattidest pürolüüsiti kaheetapilise protsessi käigus kiulise struktuuriga süsinikmaterjalid, mida samaaegselt aktiveeriti keemiliselt $ZnCl_2$-ga. Järeltöötlusena teostati süsinikmaterjalide happepesu. Optilise mikroskoopiaga saadi esialgne ülevaade kiudmattide morfoloogiast, mida hiljem kinnitati elektronmikroskoopiaga. Elektronmikroskoopia lubas samuti anda süsinikkiudude suurusele keskmistatud hinnangu. Energiadispersiivse röntgenspektroskoopia ja termogravimeetrilise analüüsi abil uuriti lisandite olemasolu süsinikmaterjalides ning seeläbi kontrolliti happepesu toimimist. Gaasiadsorptsiooni mõõtmiste abil hinnati süsiniknanokiude pooriomadusi. Töö käigus teostati süsinikust nanokiude süntees dopeeritud polümeermattidest ja uuriti valmistamistingimuste mõju sünteesitud kiude erinevatele omadustele.

Märksõnad: süsinikmaterjalid, elektroformeerimine, kiudude dopeerimine

CERCS koodid: P400 füüsikaline keemia, T140 energeetika, T150 materjalitehnoloogia

Electrospinning and Subsequent Pyrolysis of $ZnCl_2$-doped Polyacrylonitrile Mats for the Synthesis of Activated Carbon Nanofibers

In light of worldwide climate goals and advances in the field of renewable energy, there has been a rise in the demand for novel materials with specific characteristics. In particular, nanofibrous materials have claimed special attention due to their versatility in many energetics and industry applications.

Six polyacrylonitrile fiber mats doped with $ZnCl_2$ were synthesized via electrospinning. Subsequently, pyrolysis into carbon fibers was done in a two-step carbonization process concurrent with chemical activation by the dopant $ZnCl_2$ followed by a post-pyrolysis acid washing to remove impurities. Optical microscopy gave the first look into fiber mat morphology, which was later confirmed by electron microscopy. An averaged assessment of fiber width was also concluded with electron microscopy. Energy-dispersive X-ray spectroscopy along with thermogravimetric analysis was used to determine the presence of impurities and the effectiveness of acid washing. Gas adsorption measurements were performed to gauge the porosity of the carbon nanofibers. Ultimately, carbon nanofibers were synthesized from doped polymer mats, and the effect of synthesis parameters on the product fibers' properties was investigated.

Keywords: carbon materials, electrospinning, fiber doping

CERCS codes: P400 physical chemistry, T140 energy research, T150 material technology

Table of Contents

List of Abbreviations

BET - Brunauer-Emmett-Teller

BSE - Backscattered electron

CNF - Carbon nanofiber

CVD - Chemical vapor deposition

DMF - Dimethylformamide

DTG - Differential thermogravimetric

EDS - Energy-dispersive X-ray spectroscopy

IUPAC - International Union for Pure and Applied Chemistry

KTH - *Kungliga Tekniska högskolan* – Royal Institute of Technology

OM - Optical microscopy

PAN – Polyacrylonitrile

PANC – Polyacrylonitrile-based carbon

PNF - Polymer nanofiber

PSD - Pore size distribution

SDG - Sustainable development goal

SE - Secondary electron

SEM - Scanning electron microscopy

SSA - Specific surface area

TGA - Thermogravimetric analysis

Introduction

In 2015, The Sustainable Development Goals (SDG) were adopted by the United Nations General Assembly. In total 17 SDGs were named, including goals regarding affordable clean energy and climate action. These SDGs in particular outlined the estimated increase of global energy demand by 50% in the following 30 years, the continued usage of fossil-based fuels, and their effects on worldwide greenhouse gas emissions [1, 2]. Since then, most developed countries of the world have started an accelerating shift towards a more sustainable energy economy. An analysis of global trends shows rapid innovation and falling costs of renewable energy sources with a possibility to go from 15% of primary energy supply in 2015 to 63% of energy supply being from renewable energy sources in 2050. However, certain challenges have to be overcome for that plan to be realized. [3]

Amidst the aggressive shift away from fossil fuel energy and towards renewable sources, the need for energy storage is increasing rapidly. Two of the main renewable primary energy sources - wind and solar - are seasonal and not always able to sufficiently cover times of peak power consumption. Methods for long-term energy storage on a global scale are currently lacking. Aside from energy storage methods, other possibilities for alleviating stress on the electricity grid are considered, such as shifting the transportation sector from battery-operated vehicles towards hydrogen fuel cell technologies. [4]

Hydrogen shows a considerably higher gravimetric energy density than traditional fossil fuels (120 MJ kg^{-1} lower heating value for H_2 [5] vs 41.3 MJ kg^{-1} for gasoline [6]), but its volumetric energy density is much lower (11 kJ dm^{-3} lower heating value at 1 atm [5] vs 31.68 MJ dm^{-3} for gasoline [6]). The situation is exacerbated by the fact that hydrogen is not easily compressible and can leak out of most containers over time. Those problems create a need for novel hydrogen storage technologies, especially in applications related to the transportation sector i.e. vehicle fuel tanks. [6]

One possible method for hydrogen storage is physical adsorption onto porous medium. It is a mechanism by which hydrogen is stored in its molecular form on the surface of a solid material. The main advantages of physisorption over some other chemical storage methods are its complete reversibility and the small enthalpy change (1 - 10 kJ mol^{-1}) of physical adsorption – no chemical bonds are broken or created. In case of metal hydrides, the enthalpy change can cause problems

when refueling, as the process is highly exothermic. This necessitates extra modules in the storage system to dissipate heat when refueling and provide activation energy when fuel needs to be recovered from the hydride (if fueling is exothermic, then the reverse process has to be endothermic). Hydrogen storage through physical adsorption, however, relies heavily on the adsorption characteristics of the porous medium - especially specific surface area (SSA) and pore size distribution (PSD). [6]

A novel approach for hydrogen storage by physical adsorption on porous substrate is carbon nanofibers (CNFs) [7, 8]. They provide an advantage over more traditional carbon materials, as CNF mats are more readily practically applicable than bulk powders. As such, CNFs can be used in a wide variety of applications alongside hydrogen storage - lightweight thermally conductive electronic systems' materials [8–10], scaffolding materials for regenerative medicine and drug delivery [10, 11], and supercapacitor or fuel cell electrodes [8, 10, 12]. These prospects make synthesis of CNFs with fine-tuned parameters a perspective topic.

Six carbon materials were synthesized from polymer fiber mat precursors. Polymer fiber mats were electrospun from different concentrations of polyacrylonitrile (PAN) dissolved in dimethylformamide (DMF) with a small amount ($\leq$ 10 wt% of PAN) of $ZnCl_2$ added as an activating compound. The polymer fiber mats were then carbonized in a tube furnace under argon environment with a two-step temperature program. Post-pyrolysis treatment of carbon materials included acid washing with a dilute HCl solution. Initial characterization was conducted with optical microscopy (OM) to confirm a fibrous structure in the polymer fiber mats and carbon materials. After confirming the presence of a fine fibrous structure, further characterization of the carbon samples was done with thermogravimetric analysis (TGA), scanning electron microscopy (SEM), and energy-dispersive X-ray spectroscopy (EDS) methods. Gas adsorption measurements on the carbon samples were done with N_2 to gauge the carbon materials' SSA and PSD, and CO_2 for more precise characterization of micropores. Combined, the two methods can give an estimate to the successfulness of chemical activation with $ZnCl_2$.

1. Literature Review

1.1. Activated Carbon Materials

Activated carbons are a category of materials composed of a wide range of carbonized matter with different macro- and microscopic properties. All activated carbons are however related in terms of having a high SSA, variable pore size, and chemical stability. Activated carbon materials have many practical industrial applications – they are especially well known for their industrial application in different filtration and purification systems, and also to some extent in gas storage [13].

Activated carbon materials for gas storage systems is a relatively new direction which is gaining considerable industrial foothold [6]. That is partly due to both the EU countries' and USA's efforts in researching high-efficiency hydrogen gas storage both for bulk storage and for portable hydrogen fuel cell systems [4]. Among the contending technologies for the application of portable storage are high SSA carbon materials with a finely tuned porosity – for H_2 storage ultramicropores ($w < 0.7$ nm) are preferred. Such carbon materials provide a relatively light porous scaffolding structure onto which hydrogen gas can be adsorbed, especially at cryogenic temperatures and high pressures (350 - 700 bar). [6]

1.2. Carbon nanofibers

Carbon nanofibers are fibrous nanostructures of carbon with an aspect ratio of 100 or more and at least one dimension in the nanoscale [14, 15]. Contrary to the more popular carbon nanotubes, CNFs are solid structures and may either be amorphous or crystalline (graphitic). Carbon nanofibers can manifest with higher SSA than conventional carbon fibers due to their higher surface area per unit volume inherent to nanostructures. With physical or chemical activation, the SSA can be further increased by an order of magnitude. In the case of more graphitic nanofibers, elevated mechanical properties are expected due to the presence of stacked ordered structures. [14]

Due to their properties, CNFs have significant application potential in several areas, such as structural reinforcement in composites or use in carbon-based aerogels due to their low density and high SSA. Large SSA carbon nanomaterials can also be used successfully in gas sensing or as an adsorbent for pollutants in filtration systems - from exhausts, wastewater, vacuum systems etc. [14]. Alongside SSA, PSD is also an important adsorbent property, with gases requiring micro-

and mesopores (ultramicropores in case of H_2 adsorption) for adsorption and larger particles even macropores. Furthermore, CNFs mixed in a hierarchical system with traditional activated carbons have proven to be even more effective in filtrating heavy metals from water than activated carbon materials alone [16].

Main methods for acquiring CNFs are chemical vapor deposition (CVD) and pyrolysis of nanofibrous polymers. With CVD, a carbon-rich precursor is decomposed to produce elemental carbon, which is then deposited on a substrate covered with different catalysts depending on which carbon allotrope is required. Generally, it is done in a high temperature inert atmosphere and the resulting CNF properties are governed by the catalyst used and parameters of the reaction environment. In the case of polymer nanofiber (PNF) pyrolysis, the PNFs are heated in an oxygen-free environment resulting in the thermal decomposition of the precursor polymer. PNFs can be of natural origin or synthetic. [14]

1.3. Electrospinning

Electrospinning is a well-known method for synthesizing fibers from many different polymer solutions using an electric field to pull thin fibers from a solution. The resulting polymer fibers' parameters can be fine-tuned to control fiber morphology and width [17]. It is acclaimed most of all due to its versatility and ease-of-use in industrial settings. [18]

1.3.1. Experimental setup and order of work

A polymer solution is pumped through a thin capillary which also acts as a die. The capillary, also called a spinneret, is made out of an electrically conducting material - often metal. For depositing the polymer solution, a syringe with a pump is used to extrude the solution at a set speed. Volume feed speeds can range from 1 ml h^{-1} up to 100 ml h^{-1}. The conducting spinneret acts as an electrode for the generated electric field (usually between 100 and 500 kV m^{-1}), while a conducting collector plate makes up the second electrode. Charges migrate towards the surface of the polymer solution, which results in a Taylor cone. Formation of the Taylor cone occurs when electrostatic repulsive forces inside the polymer solution overcome the surface tension, deforming the otherwise round droplet into a conical shape. An electrically charged jet of polymer solution ejects from the tip of the Taylor cone and moves towards lower potential – the collector plate, which is often grounded. [17, 18]

1.3.2 Main electrospinning parameters

The characteristics of electrospun fibers are defined mainly by the polymer solution used. One of the most important parameters is the molecular weight of the polymer. A higher molecular weight will give a higher viscosity to the solution than the same concentration of the compound with a lower molecular weight. Sufficient viscosity is needed for the polymer solution jet not to break when it's being pulled by electrohydrodynamic forces. If the jet is discontinuous, then beads are formed instead of homogenous fibers. Higher molecular weight means that the polymer chains are longer, and they are more prone to entangling each other, which in turn assures the jet doesn't break. At lower viscosities, secondary thinner jets may also appear, which will result in fibers with a wide range of diameters on the collection plate. [17, 19]

Conductivity and dielectric constant also affect bead formation and the diameter of spun fibers. Conductivity is dependent on the amount of ions in the solution with a higher amount of ions in the solution resulting in a stronger elongating force – hindering bead formation and encouraging narrower fibers. A similar effect is noted with dielectric constant, which is determined by the solvent. Beading and fiber characteristics are also impacted by the processing conditions, such as solution feed rate, distance between needle and collector plate, and temperature to a smaller extent. [17, 19] The external electric force is, however, the main driving force behind the electrospinning process, as it is required to overcome the solution surface tension forces and create the Taylor cone. [19]

1.4. Pyrolysis and Chemical Activation

Pyrolysis is a process where organic materials are heated in an oxygen-free environment to induce thermal decomposition without oxidization. It is a thermochemical conversion, where both the chemical composition and physical phase of the materials change in an irreversible way. As temperature rises, the material decomposes, and the decomposition products are carried away by an inert gas flow [20]. At lower temperatures (< 573 K) water evaporation, evolution of CO, CO_2 and other gases takes place, cellulose and some other hydrocarbons depolymerize, and formation of char begins. Increasing the pyrolysis temperature (from 573 K to 773 K) speeds up the processes and induces further depolymerization, dehydration, and decarboxylation, often resulting in a tar-like precipitate [21]. After numerous conversion reactions that remove heteroatoms from the precursor material, a carbon structure remains. The resulting physical phase and extent of

graphitization are dependent on the final temperature used. Very high pyrolysis temperatures (> 1073 K) result in organization of amorphous carbon structures into graphitic carbon. [22]

Such a thermochemical conversion of carbon-rich precursors is a popular synthesis route for obtaining carbon materials. Due to the somewhat universal nature of pyrolysis reaction mechanisms, most organic mass can be used as precursor material, with already-proven options being studied extensively [23]. One such is polyacrylonitrile, an organic polymer (Figure 1) with a carbon-heavy structure (67.9% of molar mass) that decomposes instead of melting when heated.

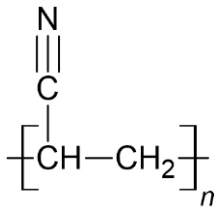

Figure 1. Condensed structural formula of PAN repeat unit.

For achieving high SSA in activated carbons, supplementary treatment is often done after or during carbonization. Chemical activation through additives in the pyrolysis mixture is a proven way to increase SSA and fine-tune PSD. Activating compounds are chosen depending on their effect on PSD, cost, and also environmental impact [23]. $ZnCl_2$ is a popular choice used for chemical activation, as it provides high SSA and microporosity when used in small concentrations [23–25]. The activation mechanism by $ZnCl_2$ is debated upon in literature, but most researchers agree it is a combination of $ZnCl_2$'s acidity in an aqueous solution (pH ~ 4) causing an etching effect, and the dehydration $ZnCl_2$ causes as a very hygroscopic compound. The dehydrating effect binds many O and H atoms from volatile surface groups and removes them as H_2O, wherein evolution of these volatile surface groups would have led to a much larger mass loss and macropore formation. [26, 27]

1.5. Microscopy Methods

1.5.1. Optical Microscopy

Optical microscopy allows the magnification of a sample's surface features through manipulation of visible light. Light reflecting from the examined sample is directed through a system of concave and convex lenses to achieve the desired transverse magnification. Although different methods can

be used to improve imaging resolution, the limiting factor for optical microscopy is defined by the physical properties of light itself [28]. It usually falls between 250 and 400 nm for modern optical microscopes [29].

1.5.2. Scanning Electron Microscopy

Scanning electron microscopy is a method for visualizing the microstructure, surface morphology, and estimating elemental composition of various electrically conductive materials. A focused electron beam scans over the examined surface in a vacuum. The interaction between the sample and focused electron beam creates particles and radiation of different origins that is used to give varying information about the sample. [30]

SEM provides two main modes of operation - secondary electron (SE) mode and backscattered electron (BSE) mode [30]. In SE mode a two-dimensional visualization of the surface microstructure topography is given. The signal is mainly constituted of low-energy electrons ($E \leq 50$ eV) created by inelastic interactions between the sample atoms' electron shells and the scanning electron beam. The SE low energies result in signal being gathered from only very close to the surface of the sample, resulting in the sample surface topography being visualized [31]. The SE detector is usually placed to one side of the vacuum chamber and exacts a slight external electric field, which is enough to capture emitted SE, but not disturb BSE or the incident beam. The resulting micrograph features topographic contrast, where deeper-down surfaces appear darker, while surfaces closer to the detector and higher up are shown as brighter. [30]

When the incident electron beam penetrates the sample surface some electrons are reflected towards the electron source at an angle greater than 90°, they are defined as BSE. This interaction is elastic and results in BSE losing some of its energy, proportional to the atomic mass of the sample atoms it is dispersed from. Detected signal is more intense when BSE are dispersed from heavier atoms. As such, BSE work mode allows an element-contrast image to be produced. [30]

1.5.3. Energy-dispersive X-ray spectroscopy

Energy-dispersive X-ray spectroscopy (EDS) allows qualitative element analysis of the sample through characteristic X-rays, which are created through relaxation of atoms excited by the probe electrons. Atoms are excited when the incident beam knocks an electron out from an inner layer of

the sample atom shell. The vacancy is filled by an electron in a higher energy state and the difference between the two energy states is radiated as a characteristic X-ray. [32]

At each point a spectrum of radiation is detected which can then be analyzed to determine the elemental composition of the sample. Repeating this process over a larger area allows the sample to be mapped in terms of elemental composition. Theoretically, quantitative analysis is possible on the same basis, but practice shows that this is not a reliable method in less-than-ideal conditions. One of the reasons for that is the large interaction volume created by high-energy incident electrons, which is in the magnitude of 1x1x1 μm. [32]

1.6. Thermogravimetric Analysis

In the TGA method a sample's mass is measured as a function of either time or temperature. The sample mass is measured under a precisely defined gas flow and temperature program depending on what sort of information is needed. During the TGA measurement, the mass of the sample will change, as it loses material through thermal decomposition and vaporization of more volatile compounds or reacts with the surrounding gas environment. These changes will produce steps in the TGA curve (and peaks in the differential thermogravimetric (DTG) curve), which can then be tied to physicochemical changes in the analyzed sample. For that, however, a basic understanding of the sample and its behavior in the selected temperature region and environment is needed. [33]

For carbon nanomaterials thermal analysis is a widely accepted method for initial characterization of their possible applications, providing useful parameters such as oxidation rate, amount of catalyst in material, activation energy etc. TGA is the fastest method for qualitatively determining the presence of impurities and comparing materials to each other. That is because all dopants and impurities create energetic defects in the carbon material matrix, which influence the dynamics and kinetics of oxidation or thermal decomposition processes (Figure 2). However, TGA results alone cannot be used for quantitative analysis, as residual mass of additives after complete oxidation of the carbon matrix does not correspond to the initial unaltered dopant compounds. [34]

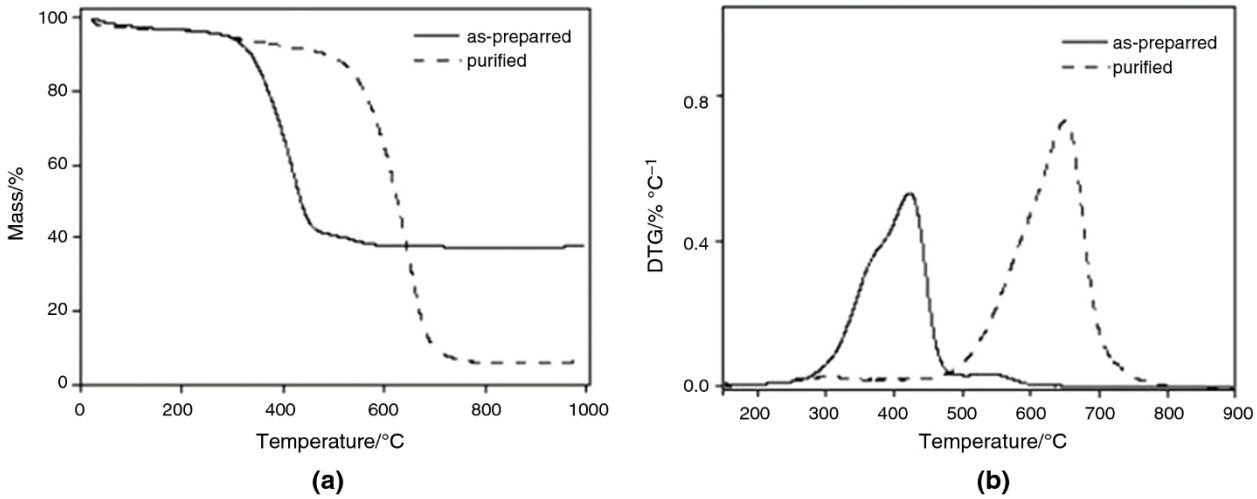

Figure 2. TGA (a) and DTG (b) curves obtained at 5 K min^{-1} in air for as-prepared and purified single-walled carbon nanotubes. [35]

1.7. Gas Adsorption

Adsorption is a term which describes when gas or liquid particles (adsorbate) adhere to a surface (adsorbent) such that the adsorbate concentration on the surface of the adsorbent is higher than in the liquid or gaseous adsorbate phase. Adsorption can be classified into physical adsorption (physisorption) and chemical adsorption (chemisorption). Physisorption is a nonspecific process which is completely reversible – physisorbed molecules always return to their original form upon desorption. Chemisorption occurs when adsorbate particles link to a reactive part of the adsorbent with enthalpy change in a comparable magnitude to that of a chemical reaction, making it a specific monolayer-limited process, often with an activation energy [36]. Classification of micro-, meso-, and macropores should also be considered when describing gas adsorption. The International Union of Pure and Applied Chemistry (IUPAC) defines them as pores with a width of < 2 nm, 2 - 50 nm, and > 50 nm, respectively. [37]

Gas adsorption measurements are a discontinuous procedure where a set volume of gas with a defined pressure and temperature is injected into the adsorption bulb. After pressure equilibrium is reached, the adsorbed amount is calculated from the difference of the actually measured and theoretically expected pressures. [36]

Adsorption data can be measured and presented in several different ways, but a standardized graphical expression is preferred for ease of comparison. Isotherms display the amount of adsorbed

gas (usually in mol g^{-1}) plotted against the equilibrium relative pressure p/p_0 (a dimensionless quantity), where p is the measurement equilibration pressure and p_0 the saturation pressure of used adsorbate at isothermal conditions (Figure 3). Isotherms can be used to give initial information about the examined material based on their shape and existence of hysteresis. [37]

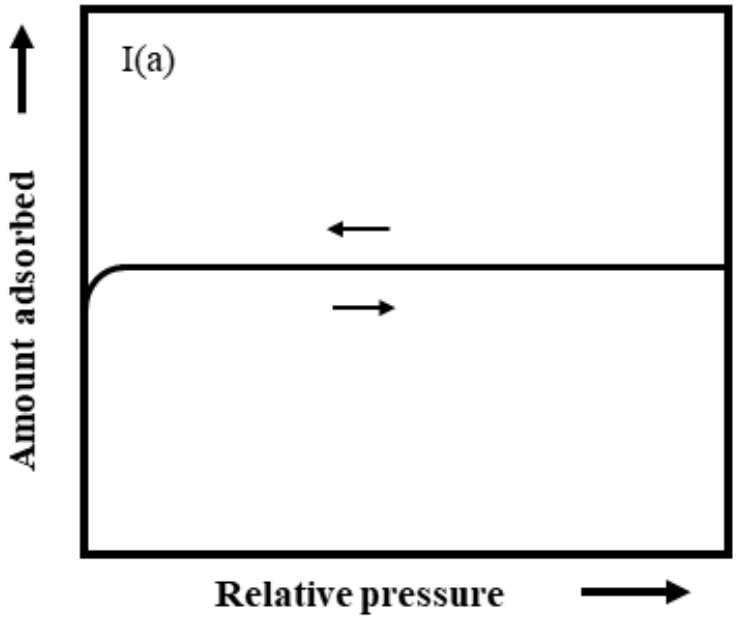

Figure 3. IUPAC type I(a) isotherm. [37]

For calculation of SSA from adsorption data, possibly the most widely used is the Brunauer-Emmett-Teller (BET) theory for multilayer adsorption of gases. It is a complement of the Langmuir theory, which presumes the adsorbent surface to be energetically homogenous, the adsorption processes to be monolayer-limited, and the interactions between adsorbate particles to be non-existent. The BET theory builds upon the Langmuir theory and stipulates that physisorbed adsorbate particles can act as sites for multilayer adsorption. It does not set an upper limit for the amount of adsorbate that can condense in case of multilayer adsorption, so the theory is not accurate at all pressures. It is, however, widely used as an industrial standard for the estimation of SSA values. [38, 39]

1.7.1. Different adsorbate gases

The standard for adsorption measurements is N_2 at 77 K, its liquefying temperature, which results in complete filling of the pores with adsorbate at higher relative pressures. At 77 K, however, gas

diffusion into micropores is relatively slow, leading to long measurement times and risk of incomplete equilibration in materials with considerable microporosity. CO_2 is a valid alternative adsorbate for these materials, as the analysis with CO_2 is done at 273 K - CO_2 does not liquefy at the pressures attainable in gas adsorption measurements. Gas diffusion at higher temperatures is faster, even if CO_2 and N_2 share a similar molecular cross-section. [36, 40]

2. Experimental

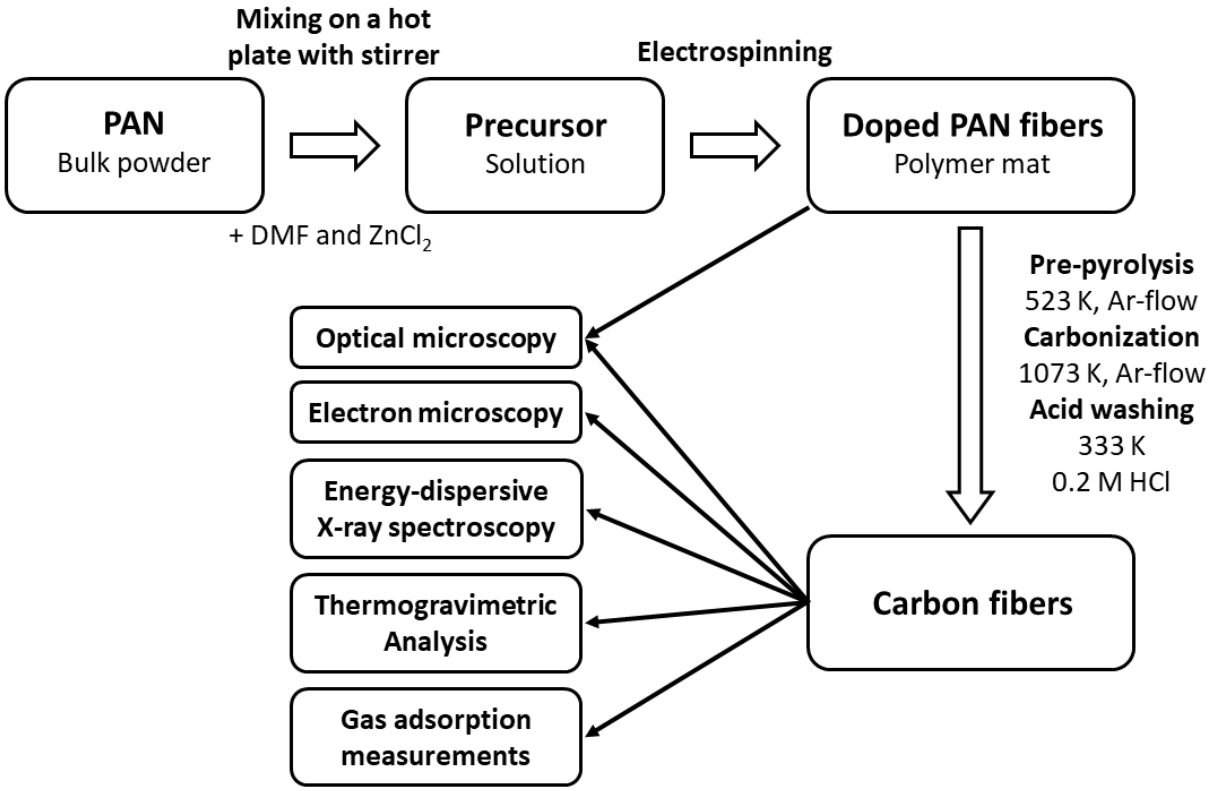

Figure 4. Block diagram of all carbon fiber synthesis steps and characterization methods used.

2.1. Electrospinning

Electrospinning was carried out with an EC-DIG (IME Technologies, Netherlands) electrospinning apparatus, which features a temperature and humidity control system, and a spinning cylindrical collector. Relative humidity of 60% and temperature of 297 K were the chosen environmental parameters. The polymer solution was made with PAN (99.2% average M_w 150000, BLDpharm) dissolved in DMF (anhydrous, 99.8%, Sigma-Aldrich) at different mass ratios, $ZnCl_2$ (anhydrous, ≥ 99.7%, Sigma-Aldrich) was added into the mixture in low concentrations (from 2.5 to 10 wt% of PAN). The solution was mixed for 24 h with the help of a magnetic stir bar, then put into a syringe and extruded at a speed of 1 ml h^{-1} from the needle with a voltage of 14 kV between the spinneret and the rotating collector ($Ø$ = 9 cm, l = 15 cm) covered with Al foil. The collector rotation speed was 500 rpm and the needle moved back and forth on a horizontal rail at a speed of 5 cm s^{-1} and turn delay of 0.5 s on either end to uniformly deposit the solution over the whole length of the collector.

Table 1. Sample nomenclature with ratio of used precursor materials. PAN:DMF ratio describes grams of PAN polymer soluted in milliliters of DMF. $ZnCl_2$:PAN ratio is the mass ratio of $ZnCl_2$ to PAN.

PAN fiber mat	Carbon material	PAN:DMF ratio	$ZnCl_2$:PAN ratio
PAN-0.05-0.1	PANC-0.05-0.1	1:20	1:10
PAN-0.1-0.05	PANC-0.1-0.05	1:10	1:20
PAN-0.1-0.1	PANC-0.1-0.1	1:10	1:10
PAN-0.2-0.025	PANC-0.2-0.025	1:5	1:40
PAN-0.2-0.05	PANC-0.2-0.05	1:5	1:20
PAN-0.2-0.1	PANC-0.2-0.1	1:5	1:10

2.2. Pyrolysis

Pyrolysis of the polymer fiber mats was done in two steps with the sample in a silica crucible put inside a TZF 12/65/550 (Carbolite, UK) three zone tube furnace. The first step comprised of a stabilizing pre-pyrolysis at 523 K with a hold time of 90 min and temperature ramp rate of 2 K min^{-1} starting from room temperature. The main carbonization process was subsequently carried out by raising the temperature at 5 K min^{-1} to 1073 K and holding for an hour. Both steps of the carbonization were done under Ar (5.0, Linde) flow with a flow rate of 100 ml min^{-1}. The tube furnace was then allowed to cool to room temperature before extracting the samples. Resulting PAN-based carbon materials (PANC) were named in accordance with the precursor PAN mat PAN:DMF:$ZnCl_2$ ratios (Table 1). Post-pyrolysis treatment with 0.2 M HCl (≥37%, Honeywell) solution and subsequent rinsing with ultrapure water (18.2 MΩ cm at 298 K, Milli-Q) was done to wash out possible impurities of thermal decomposition products of $ZnCl_2$.

2.3. Optical Microscopy

Polymer fiber mats and carbon samples were pressed between two glass slides without additional preparation and viewed under a DM1750 M (Leica, Germany) light microscope in bright field working mode. Maximum possible magnification was used, where focused images could still be obtained. Depending on the sample, it was either 100x or 150x magnification.

2.4. Scanning Electron Microscopy and Energy-Dispersive X-ray Spectroscopy

Carbon samples were transferred onto the sample holder with carbon tape and then loaded into the machine with no further preparation needed. Imaging was done with a Nova 200 SEM/FIB (FEI, USA) electron microscope in the SE work mode. The accelerating voltage was 10 kV and images were taken at 1500x - 50000x magnification.

For EDS the Ultim Max 40 (Oxford Instruments, UK) energy-dispersive spectrometer was used at 10 kV accelerating voltage. Element mapping was done at 1500x magnification to get an averaged overview of the sample composition. SEM-EDS analysis was carried out with the help of MSc Ugne Miniotaite from KTH Royal Institute of Technology, Sweden.

2.5. Thermogravimetric Analysis

The experiments were carried out on a TGA Q500 (TA Instruments, USA) thermogravimetric analyzer. The change in carbon sample mass was measured up to 1173 K under N_2 flow (3.0, Linde) and up to 1073 K under air flow. Temperature ramp rates were 10 K min^{-1} and gas flow speed 45 ml min^{-1} in both cases. TGA analysis was carried out with the help of MSc Dongkun Yu from KTH Royal Institute of Technology, Sweden.

2.6. Gas Sorption Measurements

Between 100 - 150 mg of carbon material was measured into adsorption bulbs for analysis. The samples were degassed at 573 K and under vacuum of at least 10 μbar for 24 h before adsorption measurements. For degassing and subsequent measurements, the ASAP 2020 (Micromeritics, USA) gas analyzer was used. Free space in the adsorption bulbs was measured by the gas analyzer with He before gas analysis. Measurements were done with N_2 (6.0, Linde) at a temperature of 77 K and CO_2 (5.2, Linde) at a temperature of 273 K.

3. Results and Discussion

3.1. Optical microscopy

OM confirmed the expected fibrous structure of the PAN polymer mats (Figure 5). Little to no branching of fibers could be noted and no clearly preferred orientation was observed. Due to the small width of the fibers and the layered structure of the polymer mat, fully focused images could not be obtained, and no other credible conclusions made. Precise quantification of fiber width was not possible due to inadequate resolution. This fact also necessitated the use of SEM; however, with OM an estimate could be given that the polymer fibers had a width of around 1 μm or less.

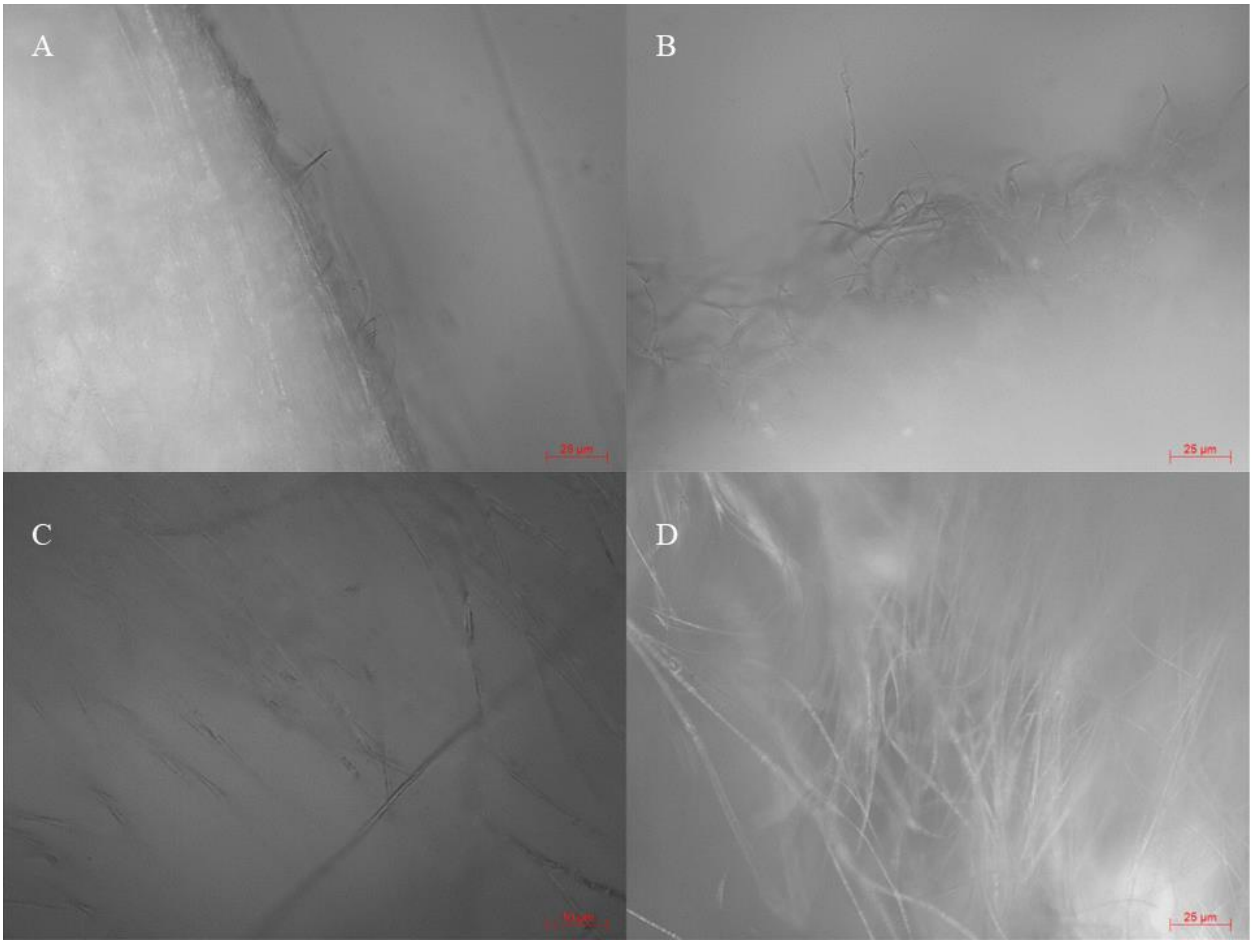

Figure 5. Images captured with an optical microscope of the PAN polymer mats. Image A depicts PAN-0.1-0.1, image B PAN-0.1-0.05, image C PAN-0.2-0.05, and image D PAN-0.2-0.1

Results of OM with carbon samples gave similar results (Figure 6). The existence of fibers was noted, confirming that the polymer mats had decomposed, not melted. PANC-0.05-0.1 was an

exception, as no fibers could be detected in the sample. Microscopy results also indicated that the carbon fibers did not have a preferred orientation. In comparison to the polymer mats, a slightly more disordered structure was observed, likely inherent to mechanical treatment received when handling the samples. Most fibers had a width of < 1 μm and could not properly be measured, but a few fibers were also seen with a width of > 1 μm. That, however, does not indicate the growth of fibers during the carbonization process. Rather it is a case of the polymer mats being more difficult to handle than carbon samples and consequently the quality of polymer mat images being slightly lower.

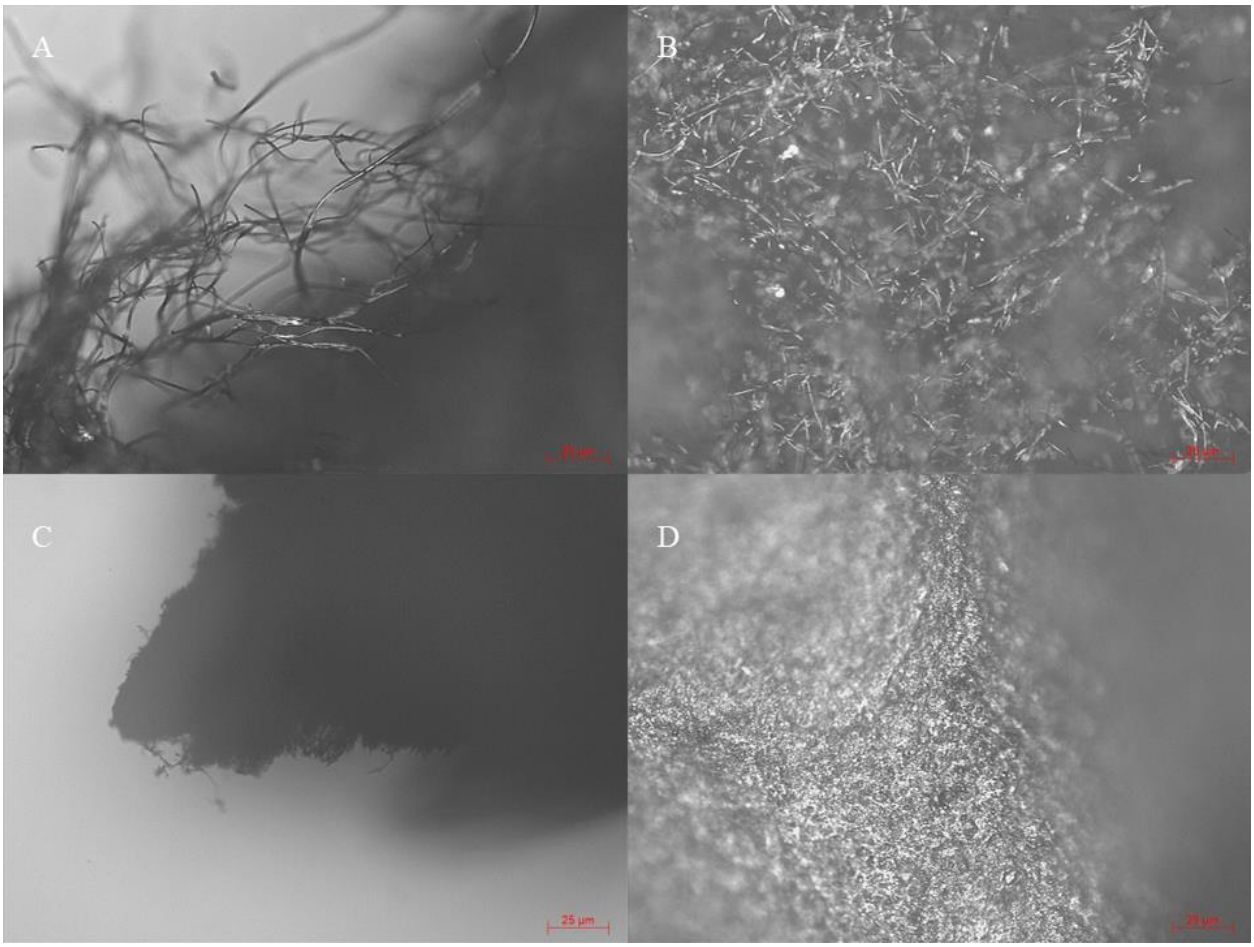

Figure 6. Images captured with an optical microscope of the PAN-derived carbon samples. PANC-0.2-0.1 in image A, PANC-0.2-0.025 in image B, PANC-0.1-0.1 in image C, and PANC-0.05-0.1 in image D.

3.2. Scanning electron microscopy

All carbon samples imaged with SEM show fibrous microstructures (Figures 7,8 and Figures from B1 to B6). All but PANC-0.05-0.1 are comprised of individual fibers, while PANC-0.05-0.1 shows a web-like entangled structure akin to molten fibers (Figure 7). This might be an effect of the low PAN concentration in DMF resulting in narrower fibers with a lower melting point than the thermal decomposition temperature of the polymer [41]. PANC-0.05-0.1 also shows larger spherical structures present, which may be the result of beading also due to the low PAN concentration in the electrospinning solution (Figure 8). Aside from PANC-0.05-0.1, other samples exhibit similar morphology, with some minor beading occurring on PANC-0.1-x series.

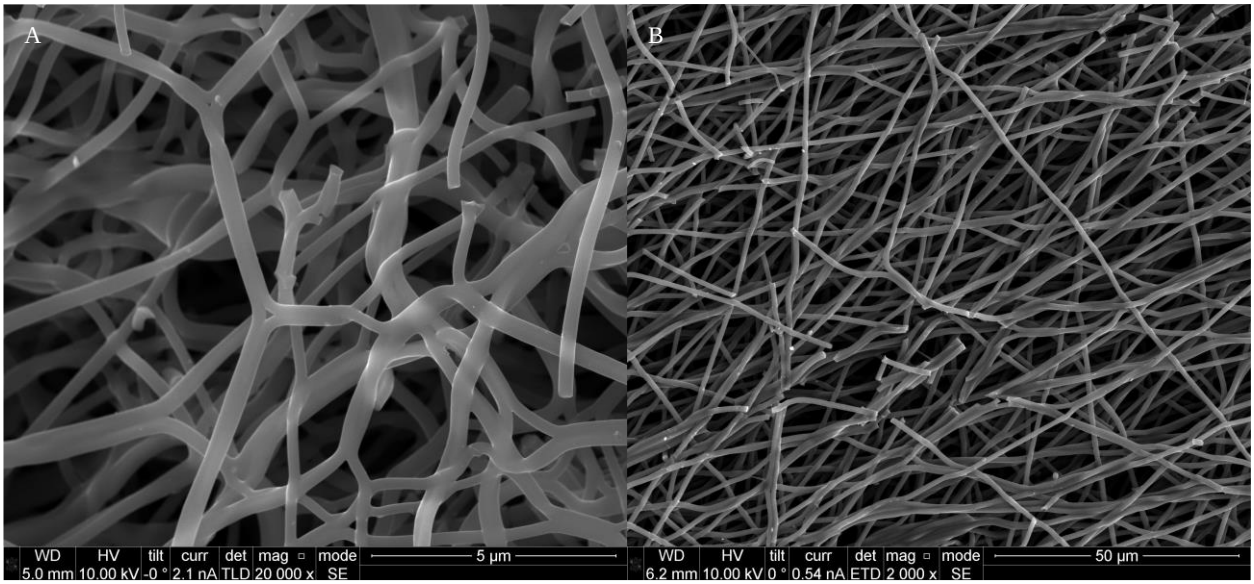

Figure 7. SEM images of carbon samples. Images taken by MSc Ugne Miniotaite from KTH. Picture A depicts close-up of PANC-0.1-0.05 microstructure, while picture B shows a wider view of PANC-0.2-0.05 carbon fiber mat morphology.

SEM images show that the carbon fibers have a width between 50 nm and 1.6 μm (Appendix B) with a clear correlation that higher PAN concentration in the electrospinning solution resulted in thicker fibers. PANC-0.05-0.1 has an average fiber width of 170 nm while for PANC-0.1-0.1 it is 300 nm and 1000 nm for PANC-0.2-0.1. Fibers of slightly different thickness are present within each sample, so the fiber thickness is not a discrete function of synthesis parameters and follows a distribution instead.

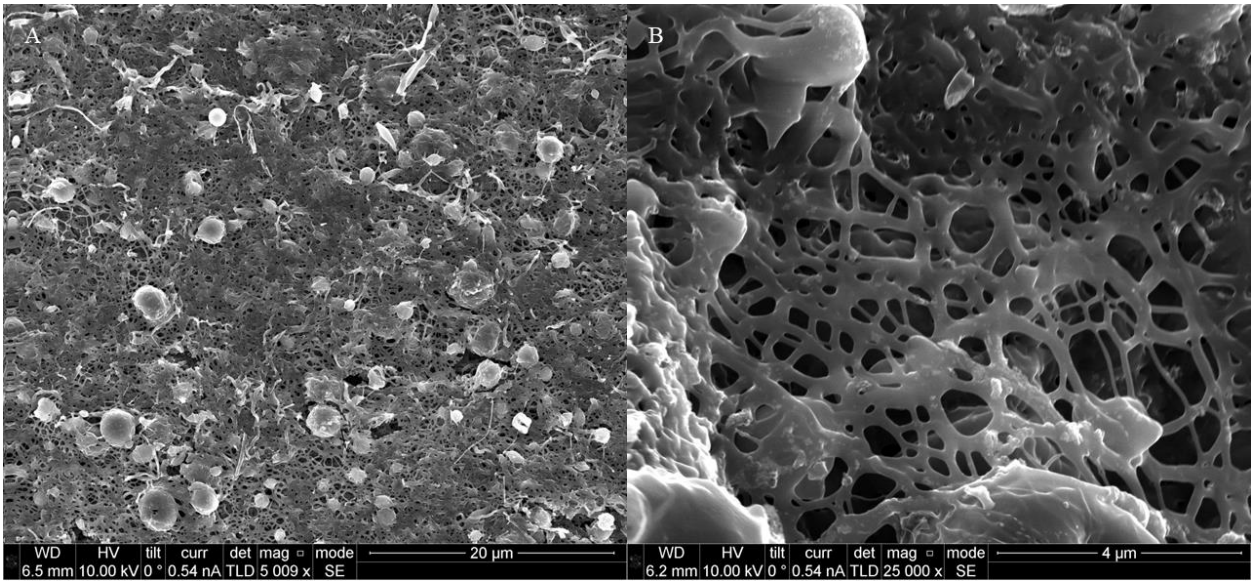

Figure 8. SEM images showing PANC-0.05-0.1 morphology. Large beads can be seen on image A, while image B shows the molten-like structure of the fibers. Images taken by MSc Ugne Miniotaite from KTH.

3.3. Energy-dispersive X-ray spectroscopy

All the carbon samples analyzed with EDS gave signals corresponding to carbon and nitrogen, as expected. All samples also had signals corresponding to oxygen and zinc with a uniform distribution over the scanned area and no concentrated sites of any one element. It can be inferred that oxygen and zinc are bound as a chemical compound - ZnO - a decomposition product of $ZnCl_2$. ZnO's existence is supported by the fact that metallic Zn is very improbable to exist in such quantities within the samples after pyrolysis. Also, no other elements are shown by EDS that could form a stable compound with Zn. As such, there is enough evidence to suggest that the acid washing was not comprehensive enough to remove all impurities from the sample. The residual ZnO most likely originates from $ZnCl_2$, the activating compound used in the synthesis process.

PANC-0.2-0.025 and PANC-0.05-0.1 also show additional elements in the EDS analysis. For PANC-0.2-0.025 it is localized signals corresponding to Ca, O and Si (Figure A4). The concentrated nature of the signal and overlapping of Ca and O-tainted areas indicate that unknown outside impurities have been introduced to the sample. The amount of impurities and their effect on the sample properties cannot be quantified by EDS. With PANC-0.05-0.1 Cl, Mg, Ca, and Si are diffusely detected across the sample (Figure A1). It is possible that these impurities are related

to the structural changes seen in SEM results, but a definitive causality cannot be established based on these results alone.

3.4. Thermogravimetric analysis

Two carbon materials were measured with TGA in air flow to evaluate the ash content of synthesized carbon samples and compare their oxidization curves (Figure 9). PANC-0.1-0.1 and PANC-0.1-0.05 reported with a similar DTG profile, except for a difference in combustion temperature, which was around 50 K lower for PANC-0.1-0.1. The TGA curves of both samples also show a slight increase of mass (1.37 percentage points for PANC-0.1-0.1 and 2.25 percentage points for PANC-0.1-0.05) after the main combustion process. The ash contents for PANC-0.1-0.1 and PANC-0.1-0.05 are 10.0 wt% and 6.1 wt% respectively. The difference in ash content and combustion temperature between samples is likely related to the amount of impurities, namely residual Zn-compounds from doping, in the carbon materials [34]. The TGA profiles of both samples are consistent with examples of carbon sample TGA curves found in literature [42–44].

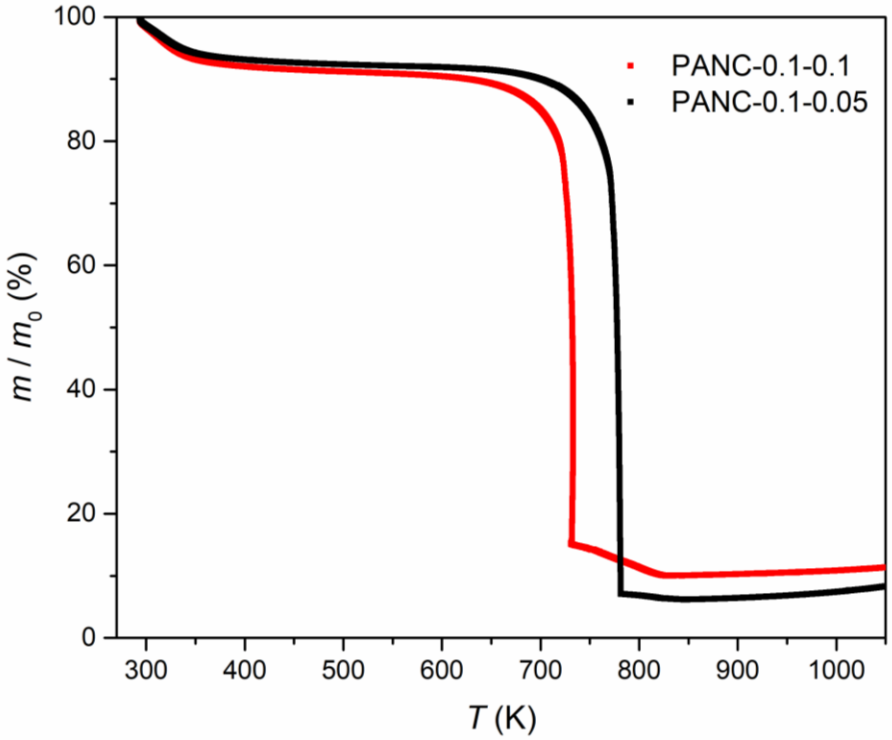

Figure 9. TGA curves for PANC-0.1-0.1 and PANC-0.1-0.05 done under air flow with a flow rate of 45 ml min^{-1} and heating rate of 10 K min^{-1}.

Samples of the same carbon materials were also analyzed with TGA in N_2 flow to further compare the two samples with same synthesis parameters except for $ZnCl_2$ concentration in the precursor solution (Figure 10). Both samples exhibit a noticeable mass loss, but the TGA and DTG profiles are noticeably different. After initial removal of humidity at $T < 400$ K both samples have a slight run-off of mass that is possibly caused by further ambient gas (air constituents) desorbing from the carbon material. PANC-0.1-0.1 continues losing mass between 400 K < T < 700 K at a steady rate, no stable plateau is established. At roughly T = 800 K the mass loss rate for PANC-0.1-0.1 rises and by the end of the experiment only 64% of the initial mass remains. For PANC-0.1-0.05 the mass loss accelerates at $T \sim 850$ K, but according to the DTG the rate is less than half of what it was for PANC-0.1-0.1. The final mass for PANC-0.1-0.05 is 82% of its initial mass. Similar TGA curves of carbon materials with mass loss in inert gas flow at high temperatures (> 700 K) have been shown in literature before by Polovina et al. when oxygen-containing functional groups were present in the carbon structure [45].

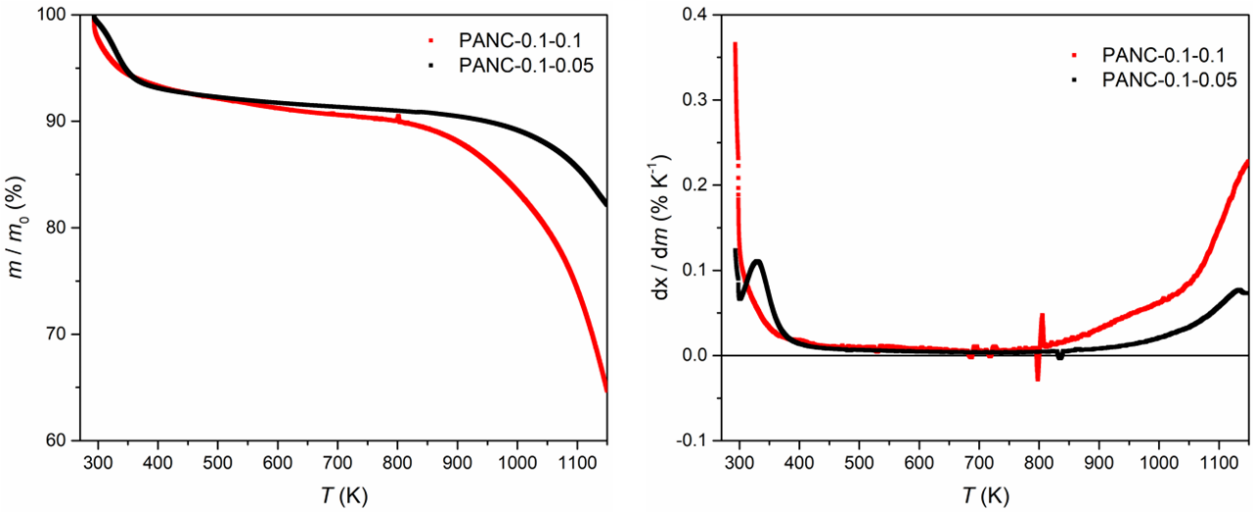

Figure 10. TGA (left) and DTG (right) profiles for PANC-0.1-0.1 and PANC-0.1-0.05 done under N_2 flow with a flow rate of 45 ml min^{-1} and heating rate of 10 K min^{-1}. Small spikes in DTG profiles between 650 < T < 850 K are due to accidental mechanical disturbances of the measurement apparatus.

3.5. Adsorption measurements

N_2 adsorption measurements were attempted on carbon samples, but for most samples the adsorption analyzer failed to reach equilibrium pressure at isothermal conditions, namely at low

p/p_0 values. With the very few successful measurements, negative adsorption isotherms were obtained (Figure 11 and Figure C1), which indicated gas desorption from the sample. Repeat measurements with higher sample mass and extra degassing on the measurement port after free space measurement with He still yielded negative isotherms with little to no improvement. BET SSA of 1 $m^2\ g^{-1}$ was reported for PANC-0.1-0.1 as the most successfully measured carbon sample.

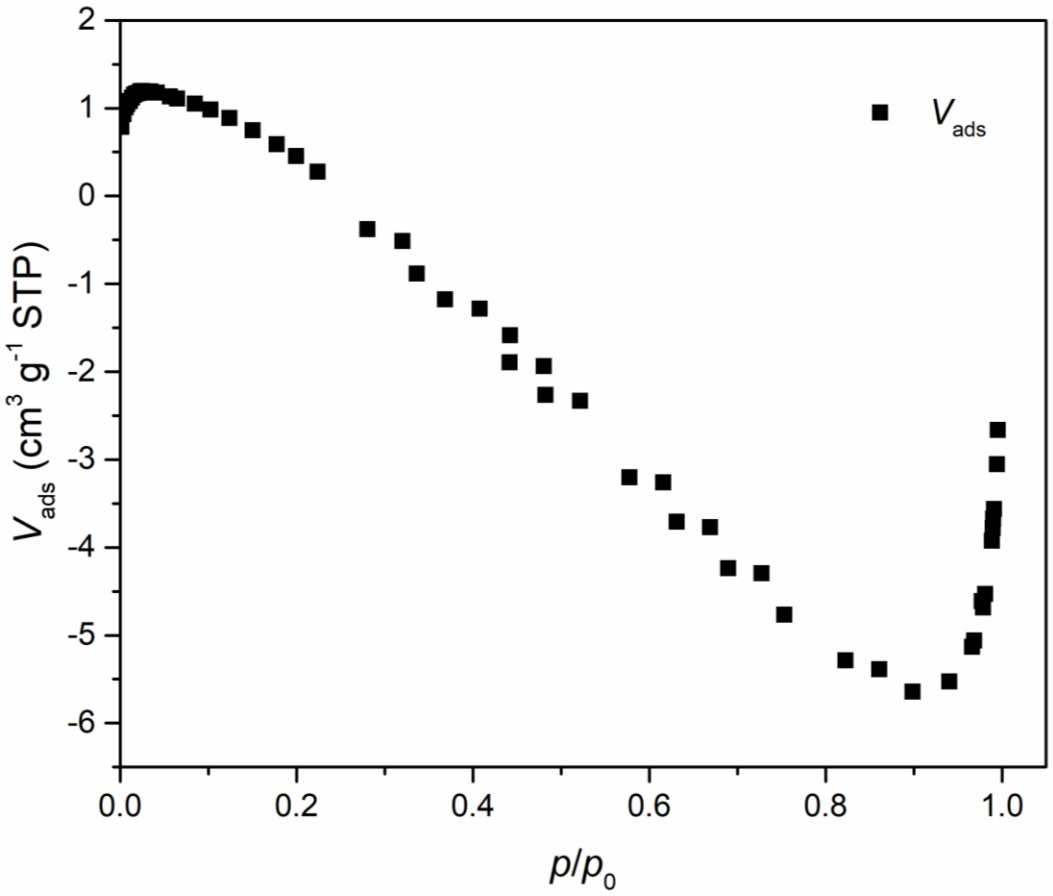

Figure 11. N_2 adsorption isotherm of PANC-0.1-0.1. Irregular isotherm shape does not correspond to any typical isotherm types as listed by IUPAC.

Measurements with CO_2 were attempted as CO_2 exhibits faster diffusion into pores due to the higher measurement temperature of 273 K and thus, CO_2 is more suitable for microporous materials or materials with narrow-necked porosity. Regardless, no consistent results were achieved over all synthesized carbon samples. Many measurement attempts failed as the samples failed pre-analysis leak tests even after prolonged degassing and switching of adsorption bulbs and flask caps. Of the analyses that were measured in the full p/p_0 range, negative isotherms were mostly received

(Figures C2, C3). Only for one material, PANC-0.1-0.1, two full adsorption isotherms were successfully measured with CO_2 corresponding to that of a microporous material (Figures C4, C5). As it was the only material and only in the case of CO_2 adsorption, it could not be considered representative of the full series.

Adsorption measurements with N_2 and CO_2 did not yield useful data that could be fit with PSD or more exact SSA calculation models. Due to the failed adsorption measurements, it can be inferred that chemical activation of the carbon fibers was not successful and $ZnCl_2$ did not work as an activating compound, or the created porosity was for the most part of the closed type.

3.6. Further Discussion

While electron and optical microscopy methods showed that the expected fibrous structure of the carbon materials was achieved, TGA results indicate, and are corroborated by EDS data, that the dopant's decomposition products were not successfully removed from the carbon nanofibers. Ash content was discovered in the same magnitude as $ZnCl_2$ added to the precursor materials while elemental analysis backs up the theory that ZnO, a thermal degradation product of $ZnCl_2$, is still left in the carbon material. The origin of oxygen required for formation of ZnO can be explained by trace oxygen not yet desorbed from the PAN structure, as $ZnCl_2$ melts and decomposes at around 565 K [26], possibly even lower if it's dispersed as small particles in a nanofiber substrate. Alternatively, the $ZnCl_2$ can decompose into metallic zinc, which will then oxidize post-pyrolysis when in contact with air. It is also possible that some defects or oxidizing functional groups have formed in the carbon structure. Both functional groups and inorganic impurities will induce energetically favorable sites in the carbon structure, where oxidization or thermal degradation can occur during TGA measurements in air or N_2 flow, respectively [34, 45]. The consistent O signal in EDS also corroborates this theory.

Washing with HCl is a standard procedure for removing inorganic compounds, such as ZnO, from the final product. HCl reacts with ZnO to produce $ZnCl_2$ (which is water-soluble and can be easily rinsed out) and H_2O. ZnO in the sample (or any other Zn-compound for that matter) denotes that HCl has not been able to react with it, therefore the ZnO is most likely encapsulated inside closed porosity of the carbon structure inaccessible to HCl. From the adsorption measurements it can be inferred that $ZnCl_2$ failed to chemically activate the carbon nanofibers, at least to an adequate extent to cause considerable open porosity.

Although the theories above could not decisively be confirmed in the scope of this thesis, many interesting questions have arisen that require further investigation. In particular, research into the optimization of $ZnCl_2$ doping and post-pyrolysis purification of the carbon fibers should be done. One possibility is to use a higher concentration of $ZnCl_2$ in the precursor solution to promote formation of slightly larger pores that are accessible to HCl in the acid washing process. Alternatively, finding a different method to activate the successfully synthesized carbon nanofibers could propose an easier solution to this problem.

Summary

Six polymer fiber mats were electrospun from different concentrations of PAN dissolved in DMF with a small amount (≤ 10 wt% of PAN) of $ZnCl_2$ added as an activating compound. The polymer fiber mats were then carbonized in a tube furnace under an argon environment with a two-step temperature program - pre-pyrolysis at 523 K and main carbonization at 1073 K. Post-pyrolysis treatment involved washing in dilute HCl solution. The carbon samples and polymer mats were initially characterized with OM, then the carbon mats subsequently with SEM to confirm a fibrous microstructure and characterize the width of carbon fibers present. EDS and TGA were used to qualitatively gauge the chemical purity of synthesized carbon samples, TGA also gave a comparison between samples with different amounts of dopant in the precursor solution. Gas adsorption measurements were attempted to evaluate the SSA and characterize the pore structure of the carbon materials.

OM showed the existence of a fibrous microstructure in both precursors and carbonized materials. Further imaging with SEM confirmed the existence of unordered carbon fibers with a width between 50 nm and 1.6 μm with varying lengths. EDS showed the existence of different impurities and gave reason to believe that ZnO, the thermal decomposition product of $ZnCl_2$, had not been removed from the carbon materials in post-pyrolysis acid washing. With TGA the ash content of the carbon materials was measured, and the presence of energetically active sites within the carbon microstructure showed. Gas adsorption measurements with N_2 and CO_2 at 77 K and 273 K, respectively, failed to give an accurate representation of the carbon materials' SSA or PSD, but did confirm that an expected high SSA and accessible porosity in the structure of carbon fibers was not achieved.

It was concluded that carbon nanofibers were successfully synthesized, but chemical activation with $ZnCl_2$ failed to create considerable open porosity. This leaves several potential directions for further research. Optimization of the synthesis route can be undertaken, or alternatively finding completely new pathways to activate the carbon nanofibers that were synthesized from PAN precursor.

Kokkuvõte

Kuus polümeermatti elektroformeeriti sünteesilahustest, kus oli eri kontsentratsioonides PAN-i lahustatud DMF-is väikese hulga (≤ 10 massi% PAN-ist) $ZnCl_2$ lisandiga. Polümeerkiust matid karboniseeriti seejärel toruahjus argoonivoolus kaheastmelise temperatuuriprogrammi abil - eelpürolüüs 523 K juures ning karboniseerimine 1073 K temperatuuril. Pürolüüsijärgselt töödeldi sünteesitud süsinikmaterjale lahendatud HCl lahuses. Polümeer- ja süsinikmatte karakteriseeriti esialgu OM-iga, seejärel süsinikkiudmatte SEM-iga, et kinnitada materjalide kiudjas mikrostruktuur ja karakteriseerida süsinikkiude. Viidi läbi EDS ja TGA analüüsid, et hinnata süsinikkiumattide keemilist puhtust ning TGA võimaldas võrrelda kahte erineva dopandi hulgaga proovi. Gaasisorptsiooni analüüse teostati, et hinnata süsinikmaterjalide eripinda ja pooristruktuuri.

OM kinnitas kiudja struktuuri olemasolu nii polümeerkiudmattides kui ka karboniseeritud materjalides. Edasine uurimine SEM-i abil näitas vahelduva pikkusega eelistatud orientatsioonita süsinikkiudude olemasolu, mille laius jäi 50 nm ning 1,6 μm vahemikku. EDS näitas mitmesuguste lisandite olemasolu ning andis alust uskuda, et happepesu ei olnud süsinikmaterjalist eemaldanud ZnO-i, mis on $ZnCl_2$-i laguprodukt. TGA abil hinnati süsinike tuhasisaldust ja kinnitati energeetiliselt aktiivsete tsentrite olemasolu süsinikstruktuuris. Gaasisorptsiooni analüüsid N_2 ja CO_2-ga vastavalt temperatuuridel 77 K ja 273 K ei suutnud anda täpset ettekujutust süsinikmaterjalide eripinnast ega poorijaotusest, kuid kinnitasid, et süsinikmaterjali keemiline aktiveerimine ei loonud märkimisväärset avatud poorsust ega ootuspärast kõrget eripinda.

Töö käigus sünteesiti edukalt süsinikust nanokiud, aga nende keemiline aktiveerimine $ZnCl_2$-ga ebaõnnestus. Antud uurimuse tulemuste põhjal on võimalik püstitada mitmeid edasisi uurimisküsimusi. Eeskätt tasub optimeerida olemasoleva sünteesiraja toimimist, et tagada keemilise aktiveerimise õnnestumine ja lõpp-produkti keemiline puhtus. Alternatiivselt võib välja töötada täiesti eraldiseisva viisi edukalt valmis sünteesitud süsiniknanokiudude aktiveerimiseks.

References

1. Goal 7 | Department of Economic and Social Affairs. https://sdgs.un.org/goals/goal7. Accessed 16 May 2023

2. Goal 13 | Department of Economic and Social Affairs. https://sdgs.un.org/goals/goal13. Accessed 16 May 2023

3. Gielen D, Boshell F, Saygin D, et al (2019) The role of renewable energy in the global energy transformation. Energy Strategy Reviews 24:38–50. https://doi.org/10.1016/j.esr.2019.01.006

4. Staffell I, Scamman D, Velazquez Abad A, et al (2019) The role of hydrogen and fuel cells in the global energy system. Energy Environ Sci 12:463–491. https://doi.org/10.1039/C8EE01157E

5. Dawood F, Anda M, Shafiullah GM (2020) Hydrogen production for energy: An overview. International Journal of Hydrogen Energy 45:3847–3869. https://doi.org/10.1016/j.ijhydene.2019.12.059

6. Hirscher M (2010) Handbook of hydrogen storage: new materials for future energy storage. Wiley-VCH, Weinheim

7. Kim B-J, Lee Y-S, Park S-J (2008) A study on the hydrogen storage capacity of Ni-plated porous carbon nanofibers. International Journal of Hydrogen Energy 33:4112–4115. https://doi.org/10.1016/j.ijhydene.2008.05.077

8. Ruiz-Cornejo JC, Sebastián D, Lázaro MJ (2020) Synthesis and applications of carbon nanofibers: a review. Reviews in Chemical Engineering 36:493–511. https://doi.org/10.1515/revce-2018-0021

9. Hammel E, Tang X, Trampert M, et al (2004) Carbon nanofibers for composite applications. Carbon 42:1153–1158. https://doi.org/10.1016/j.carbon.2003.12.043

10. Zhou X, Wang Y, Gong C, et al (2020) Production, structural design, functional control, and broad applications of carbon nanofiber-based nanomaterials: A comprehensive review. Chemical Engineering Journal 402:126189. https://doi.org/10.1016/j.cej.2020.126189

11. Tran PA, Zhang L, Webster TJ (2009) Carbon nanofibers and carbon nanotubes in regenerative medicine. Advanced Drug Delivery Reviews 61:1097–1114. https://doi.org/10.1016/j.addr.2009.07.010

12. Azwar E, Wan Mahari WA, Chuah JH, et al (2018) Transformation of biomass into carbon nanofiber for supercapacitor application – A review. International Journal of Hydrogen Energy 43:20811–20821. https://doi.org/10.1016/j.ijhydene.2018.09.111

13. Sinha P, Banerjee S, Kar KK (2020) Characteristics of Activated Carbon. In: Kar KK (ed) Handbook of Nanocomposite Supercapacitor Materials I. Springer International Publishing, Cham, pp 125–154

14. Sharma R, Kar KK (2020) Characteristics of Carbon Nanofibers. In: Kar KK (ed) Handbook of Nanocomposite Supercapacitor Materials I. Springer International Publishing, Cham, pp 215–245

15. Tanioka A, Takahashi M (2016) Nanofibers. In: The Society Of Fiber Science And Te J (ed) High-Performance and Specialty Fibers. Springer Japan, Tokyo, pp 273–283

16. Chakraborty A, Deva D, Sharma A, Verma N (2011) Adsorbents based on carbon microfibers and carbon nanofibers for the removal of phenol and lead from water. Journal of Colloid and Interface Science 359:228–239. https://doi.org/10.1016/j.jcis.2011.03.057

17. Wendorff JH, Agarwal S, Greiner A (2012) Electrospinning: materials, processing, and applications. Wiley-VCH, Weinheim, Germany

18. Xue J, Wu T, Dai Y, Xia Y (2019) Electrospinning and Electrospun Nanofibers: Methods, Materials, and Applications. Chem Rev 119:5298–5415. https://doi.org/10.1021/acs.chemrev.8b00593

19. Ramakrishna S (2005) An introduction to electrospinning and nanofibers. World Scientific, Hackensack, NJ

20. Tadda MA, Ahsan A, Shitu A, et al (2016) A review on activated carbon: process, application and prospects. 2:7–13

21. Shafizadeh F (1982) Introduction to pyrolysis of biomass. Journal of Analytical and Applied Pyrolysis 3:283–305. https://doi.org/10.1016/0165-2370(82)80017-X

22. Tomczyk A, Sokołowska Z, Boguta P (2020) Biochar physicochemical properties: pyrolysis temperature and feedstock kind effects. Rev Environ Sci Biotechnol 19:191–215. https://doi.org/10.1007/s11157-020-09523-3

23. Deng J, Li M, Wang Y (2016) Biomass-derived carbon: synthesis and applications in energy storage and conversion. Green Chem 18:4824–4854. https://doi.org/10.1039/C6GC01172A

24. Demiral İ, Aydın Şamdan C, Demiral H (2016) Production and characterization of activated carbons from pumpkin seed shell by chemical activation with $ZnCl_2$. Desalination and Water Treatment 57:2446–2454. https://doi.org/10.1080/19443994.2015.1027276

25. Varila T, Bergna D, Lahti R, et al (2017) Activated carbon production from peat using ZnCl2: Characterization and applications. BioRes 12:8078–8092. https://doi.org/10.15376/biores.12.4.8078-8092

26. Li B, Hu J, Xiong H, Xiao Y (2020) Application and Properties of Microporous Carbons Activated by $ZnCl_2$: Adsorption Behavior and Activation Mechanism. ACS Omega 5:9398–9407. https://doi.org/10.1021/acsomega.0c00461

27. Duan G, Zhao L, Chen L, et al (2021) ZnCl $_2$ regulated flax-based porous carbon fibers for supercapacitors with good cycling stability. New J Chem 45:22602–22609. https://doi.org/10.1039/D1NJ04667E

28. Mertz J (2019) Introduction to optical microscopy, Second edition. Cambridge University Press, Cambridge, United Kingdom ; New York, NY

29. Wilson M, DeRose J, Greb C (2023) Microscope Resolution: Concepts, Factors and Calculation

30. Zhou W, Apkarian R, Wang ZL, Joy D (2006) Fundamentals of Scanning Electron Microscopy (SEM). In: Zhou W, Wang ZL (eds) Scanning Microscopy for Nanotechnology. Springer New York, New York, NY, pp 1–40

31. Shih A, Yater J, Hor C, Abrams R (1997) Secondary electron emission studies. Applied Surface Science 111:251–258. https://doi.org/10.1016/S0169-4332(96)00729-5

32. Goodhew PJ, Humphreys FJ, Beanland R (2001) Electron microscopy and analysis, 3rd ed. Taylor & Francis, London ; New York

33. Bottom R (2008) Thermogravimetric Analysis. In: Gabbott P (ed) Principles and Applications of Thermal Analysis. Blackwell Publishing Ltd, Oxford, UK, pp 87–118

34. Bannov AG, Popov MV, Kurmashov PB (2020) Thermal analysis of carbon nanomaterials: advantages and problems of interpretation. J Therm Anal Calorim 142:349–370. https://doi.org/10.1007/s10973-020-09647-2

35. Musumeci AW, Silva GG, Martens WN, et al (2007) Thermal decomposition and electron microscopy studies of single-walled carbon nanotubes. J Therm Anal Calorim 88:885–891. https://doi.org/10.1007/s10973-006-7563-9

36. Rouquerol F, Rouquerol J, Sing KSW, et al (2014) Adsorption by powders and porous solids: principles, methodology and applications, Second edition. Elsevier/AP, Amsterdam

37. Thommes M, Kaneko K, Neimark AV, et al (2015) Physisorption of gases, with special reference to the evaluation of surface area and pore size distribution (IUPAC Technical Report). Pure and Applied Chemistry 87:1051–1069. https://doi.org/10.1515/pac-2014-1117

38. Atkins PW, De Paula J, Keeler J (2018) Atkins' Physical chemistry, Eleventh edition. Oxford University Press, Oxford, United Kingdom ; New York, NY

39. Brunauer S, Emmett PH, Teller E (1938) Adsorption of Gases in Multimolecular Layers. J Am Chem Soc 60:309–319. https://doi.org/10.1021/ja01269a023

40. Jagiello J, Thommes M (2004) Comparison of DFT characterization methods based on N2, Ar, CO2, and H2 adsorption applied to carbons with various pore size distributions. Carbon 42:1227–1232. https://doi.org/10.1016/j.carbon.2004.01.022

41. Krigbaum WR, Tokita N (1960) Melting point depression study of polyacrylonitrile. J Polym Sci 43:467–488. https://doi.org/10.1002/pol.1960.1204314217

42. Peng Z, Guo Z, Chu W, Wei M (2016) Facile synthesis of high-surface-area activated carbon from coal for supercapacitors and high CO_2 sorption. RSC Adv 6:42019–42028. https://doi.org/10.1039/C5RA26044B

43. Mansfield E, Kar A, Hooker SA (2010) Applications of TGA in quality control of SWCNTs. Anal Bioanal Chem 396:1071–1077. https://doi.org/10.1007/s00216-009-3319-2

44. Farivar F, Yap PL, Hassan K, et al (2021) Unlocking thermogravimetric analysis (TGA) in the fight against "Fake graphene" materials. Carbon 179:505–513. https://doi.org/10.1016/j.carbon.2021.04.064

45. Polovina M, Babić B, Kaluderović B, Dekanski A (1997) Surface characterization of oxidized activated carbon cloth. Carbon 35:1047–1052. https://doi.org/10.1016/S0008-6223(97)00057-2

46. Jagiello J, Ania C, Parra JB, Cook C (2015) Dual gas analysis of microporous carbons using 2D-NLDFT heterogeneous surface model and combined adsorption data of N2 and CO2. Carbon 91:330–337. https://doi.org/10.1016/j.carbon.2015.05.004

Acknowledgements

First and foremost, as most theses go, I have to thank my supervisor - Rasmus Palm - for his gargantuan efforts in providing both a challenging, but at the same time a very supportive and rewarding working environment. I also express major gratitude towards prof. Lust's Chair of Physical Chemistry at Tartu (especially prof. Thomas Thomberg for his insight into electrospinning) and prof. Månsson's SMaRT group at KTH in Stockholm - it has been a pleasure to work with and be guided by such innovative people. Finally, on a more personal note, I'd like to thank the two people who I consider to be main reason I didn't burn out halfway through this endeavour - Anett for redefining to me what "emotional support" can truly mean, and Elise for being an everlasting annoying constant throughout all five of the years I've spent in academia.

Appendix A. Energy-Dispersive X-ray Spectroscopy Results

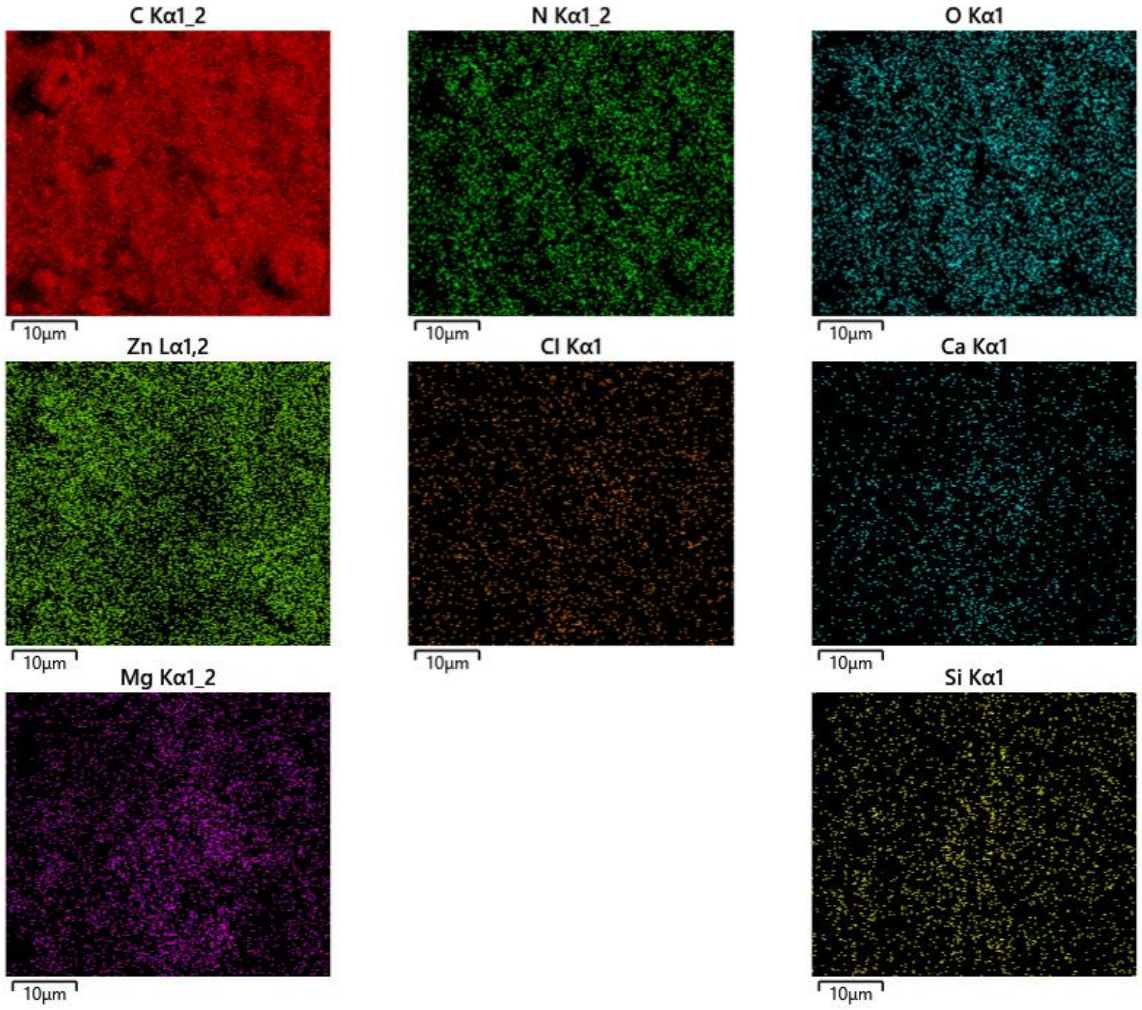

Figure A1. EDS results of PANC-0.05-0.1.

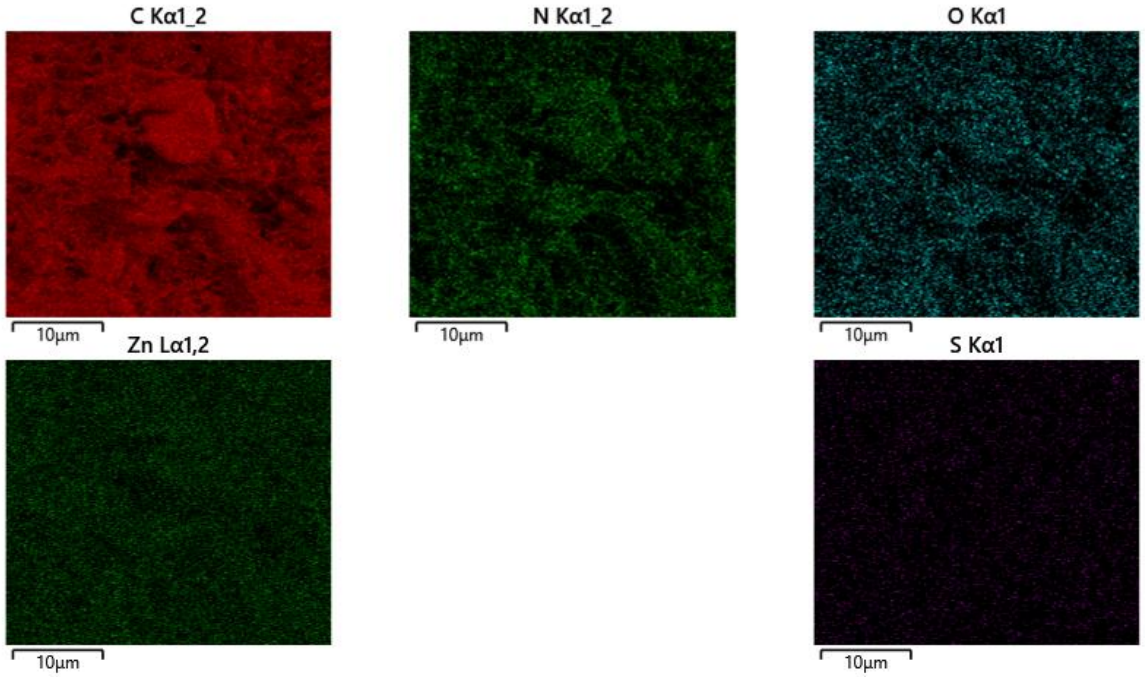

Figure A2. EDS results of PANC-0.1-0.05.

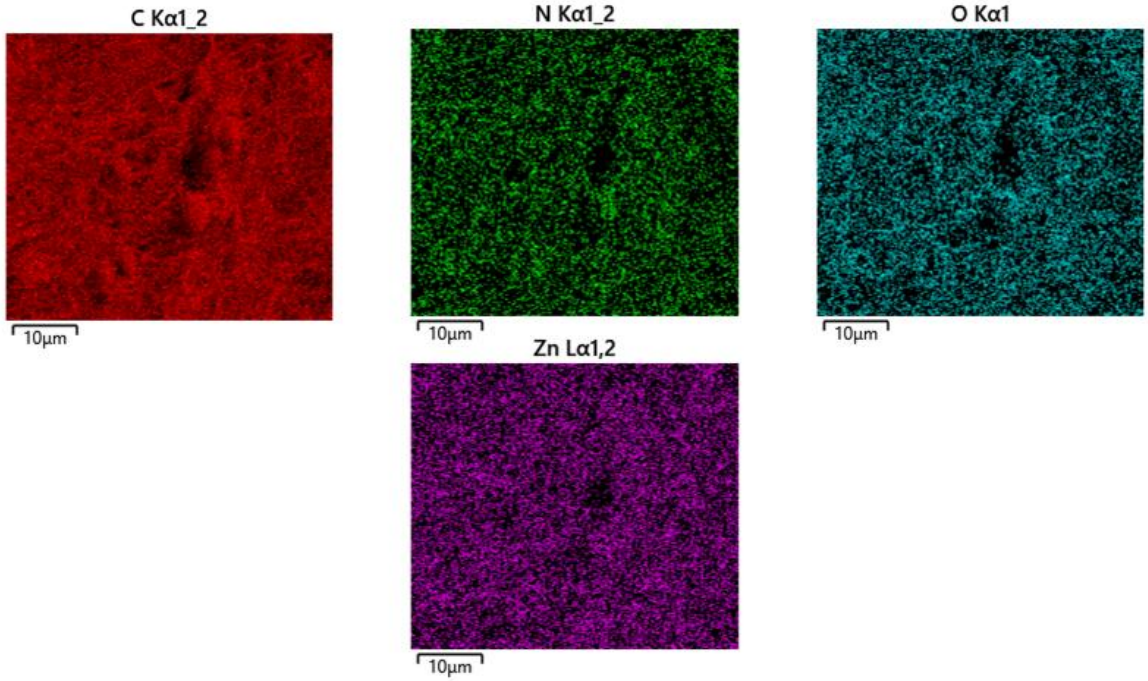

Figure A3. EDS results of PANC-0.1-0.1.

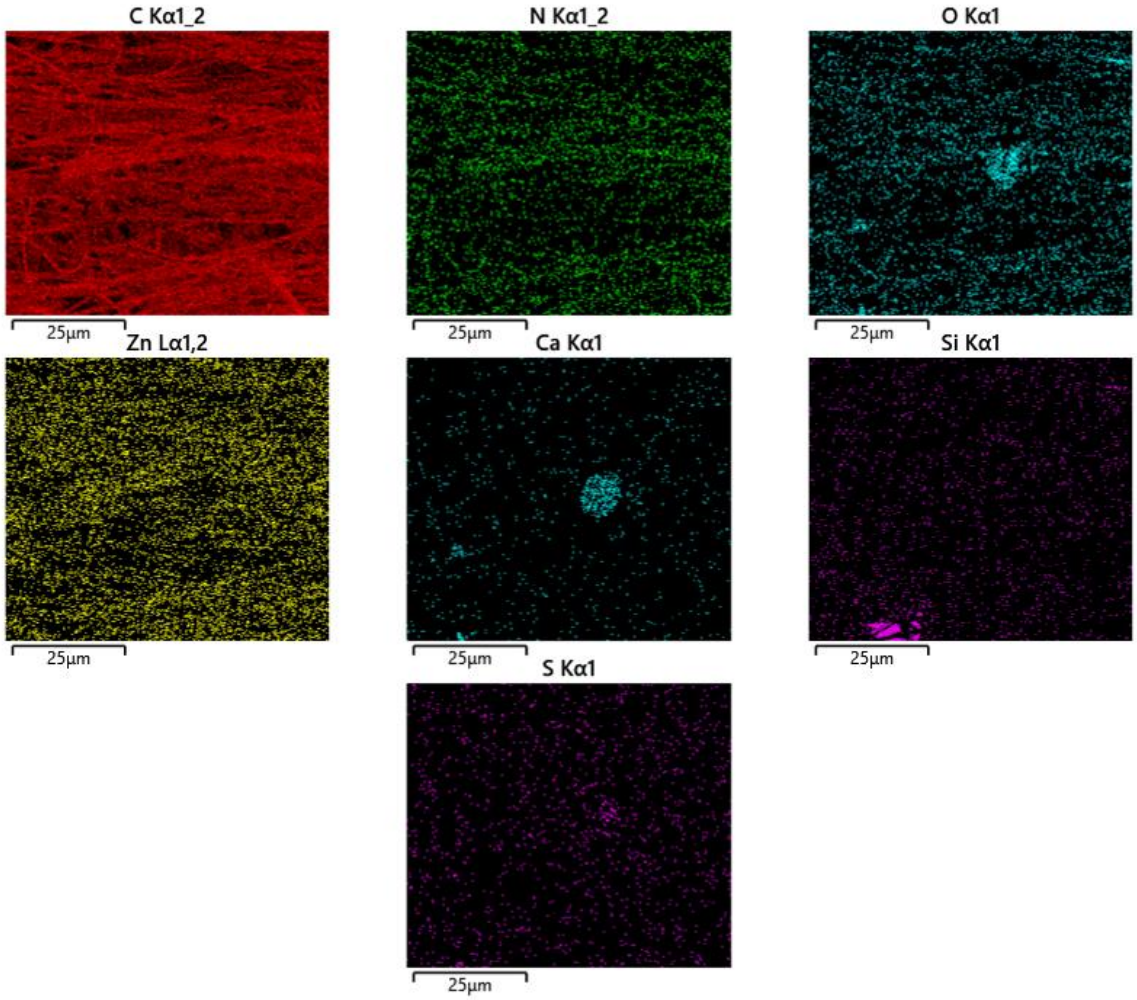

Figure A4. EDS results of PANC-0.2-0.025.

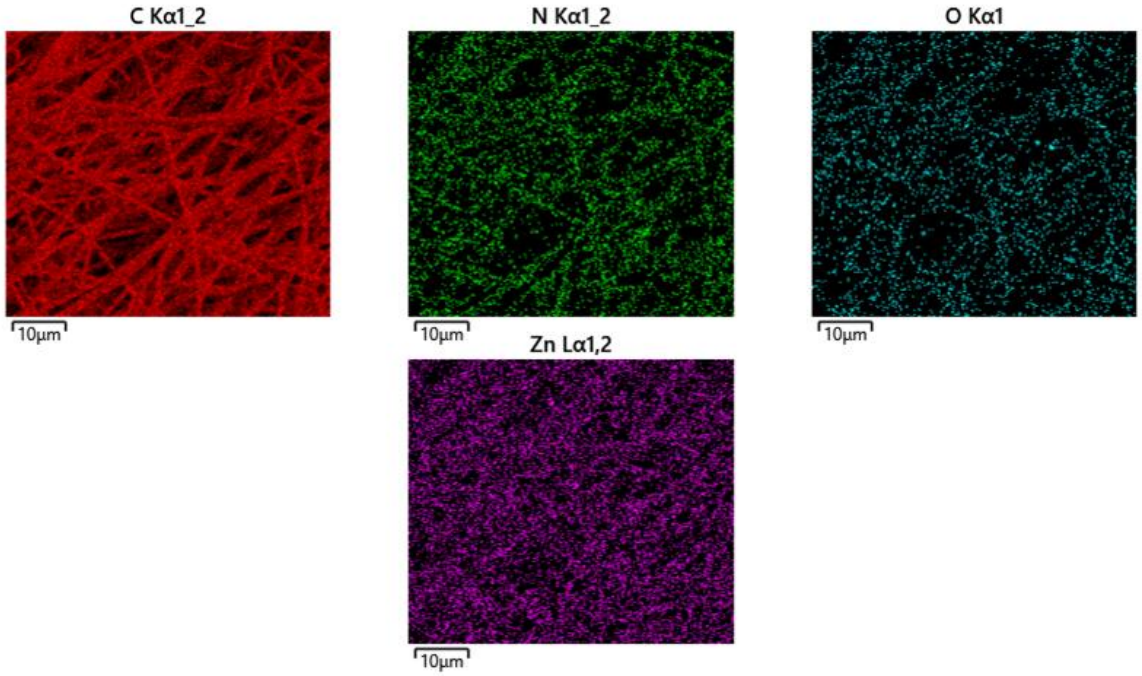

Figure A5. EDS results of PANC-0.2-0.05.

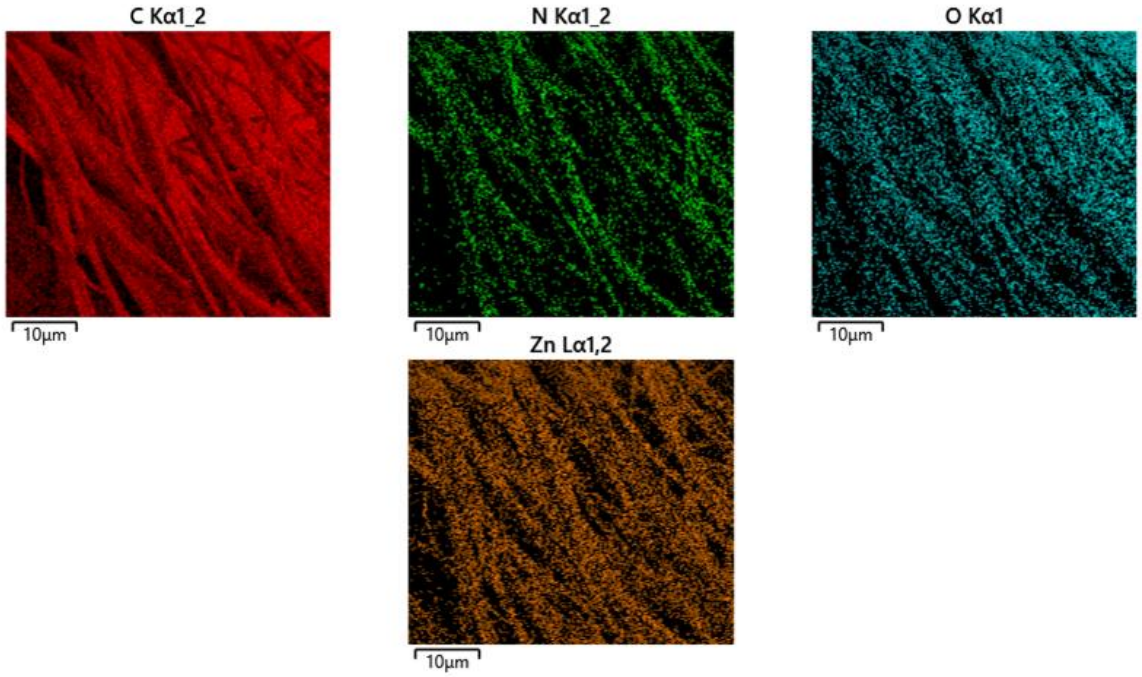

Figure A6. EDS results of PANC-0.2-0.1.

Appendix B. Carbon Fiber Width Distribution Analysis Based on SEM Images

Fiber widths' histograms were fitted with Gaussian distribution, uncertainty presented with a confidence interval of 95 %.

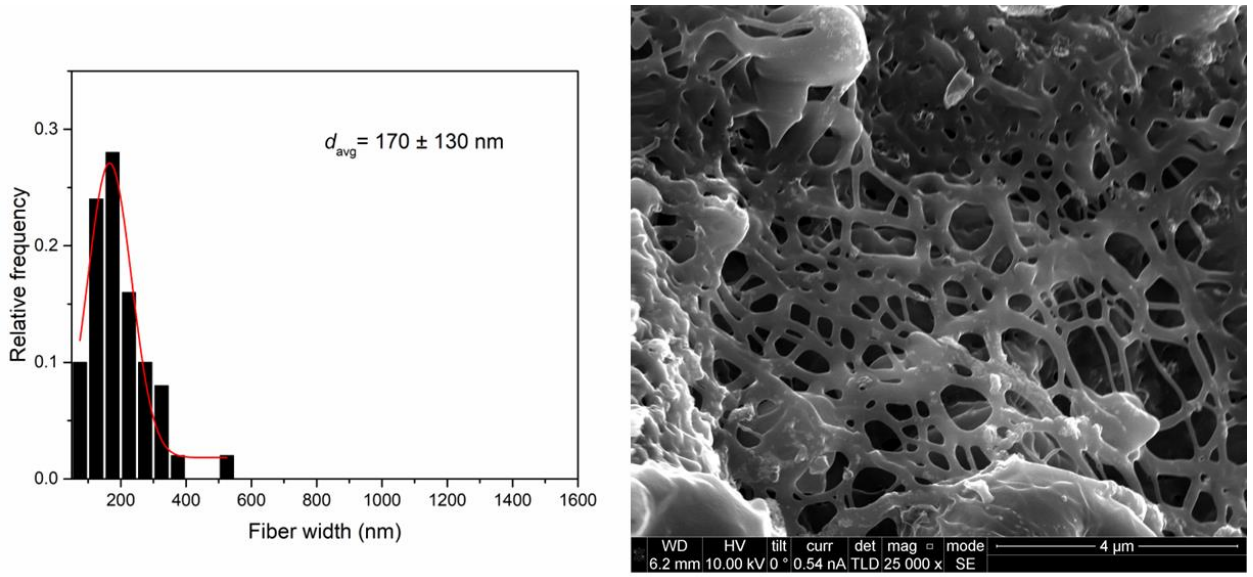

Figure B1. Carbon fiber size distribution plot for PANC-0.05-0.1.

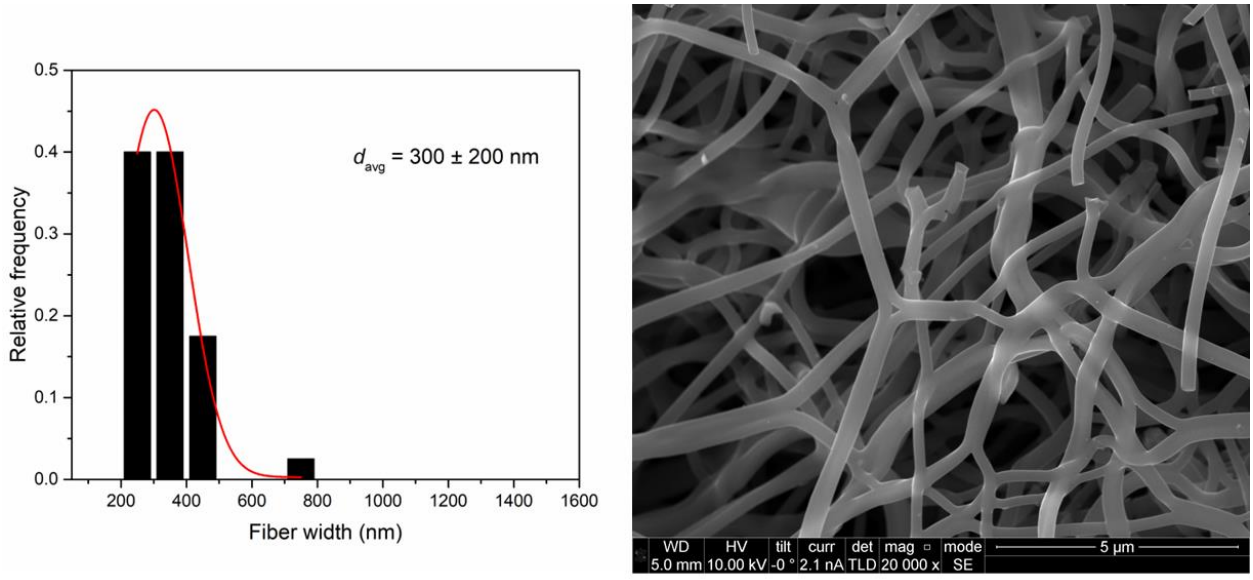

Figure B2. Carbon fiber size distribution plot for PANC-0.1-0.05.

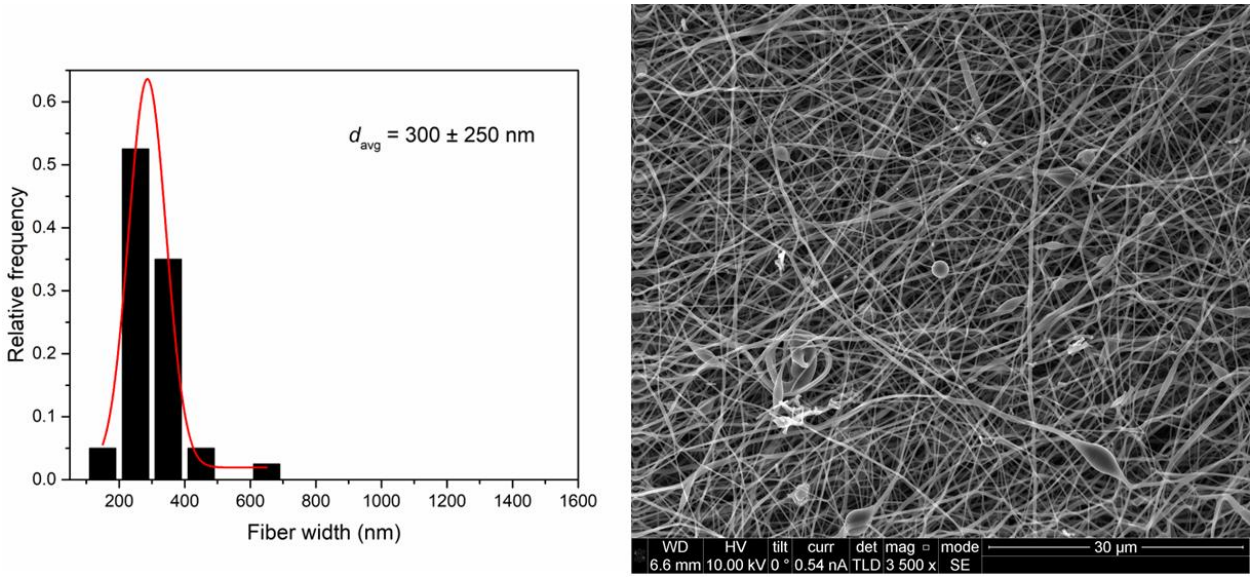

Figure B3. Carbon fiber size distribution plot for PANC-0.1-0.1.

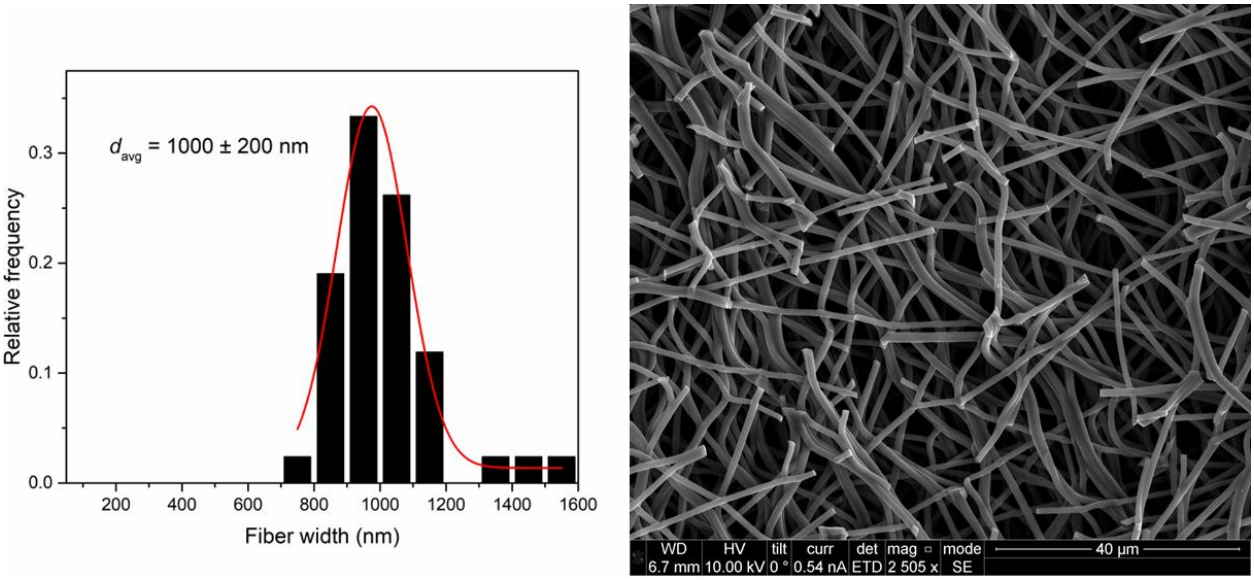

Figure B4. Carbon fiber size distribution plot for PANC-0.2-0.025.

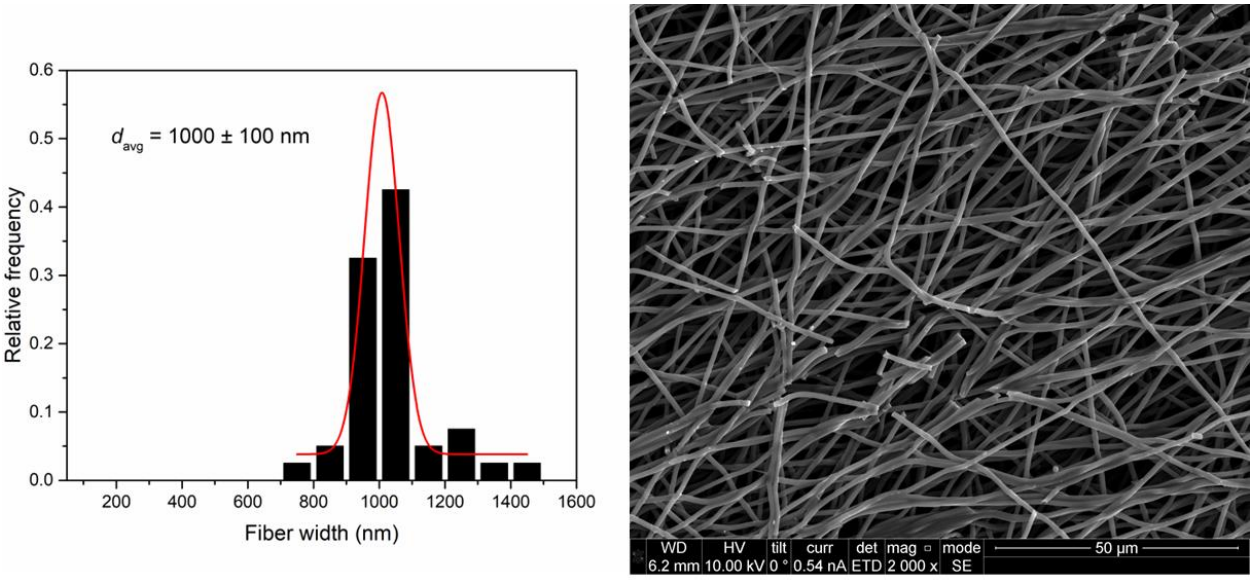

Figure B5. Carbon fiber size distribution plot for PANC-0.2-0.05.

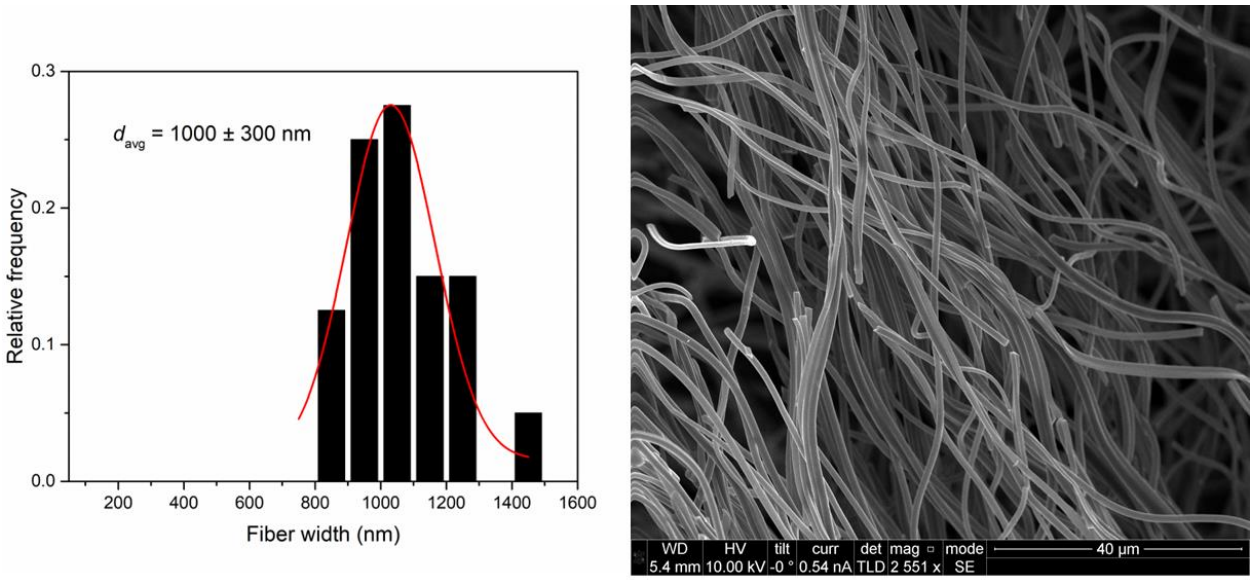

Figure B6. Carbon fiber size distribution plot for PANC-0.2-0.1.

Appendix C. Completed Adsorption Measurements' Isotherms

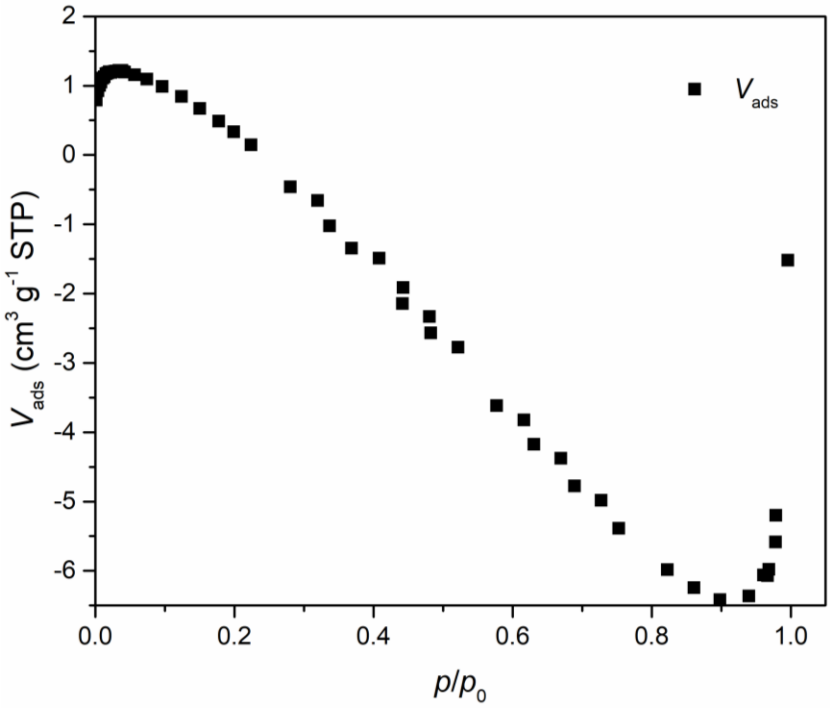

Figure C1. N_2 adsorption measurement isotherm of PANC-0.1-0.1.

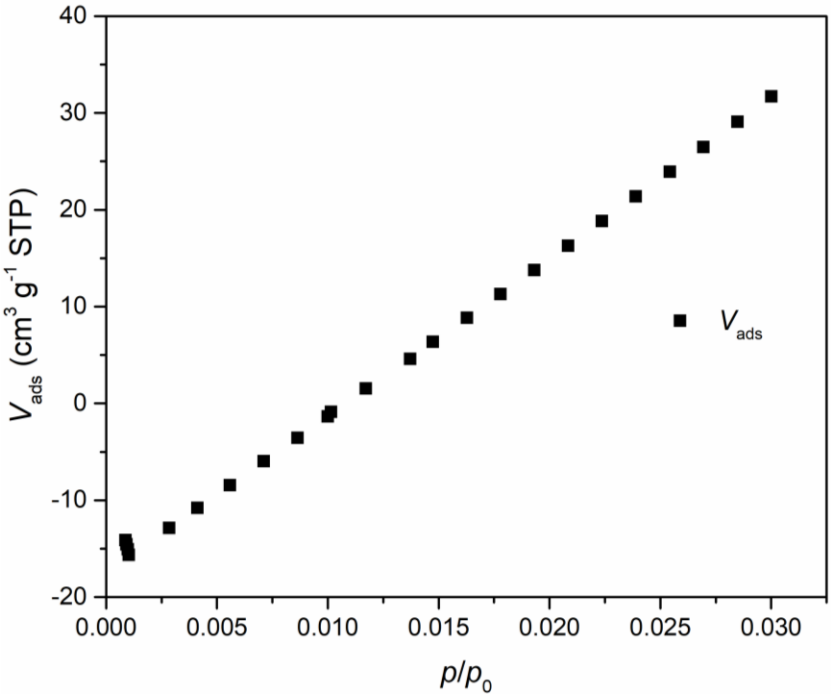

Figure C2. CO_2 adsorption measurement isotherm of PANC-0.2-0.1.

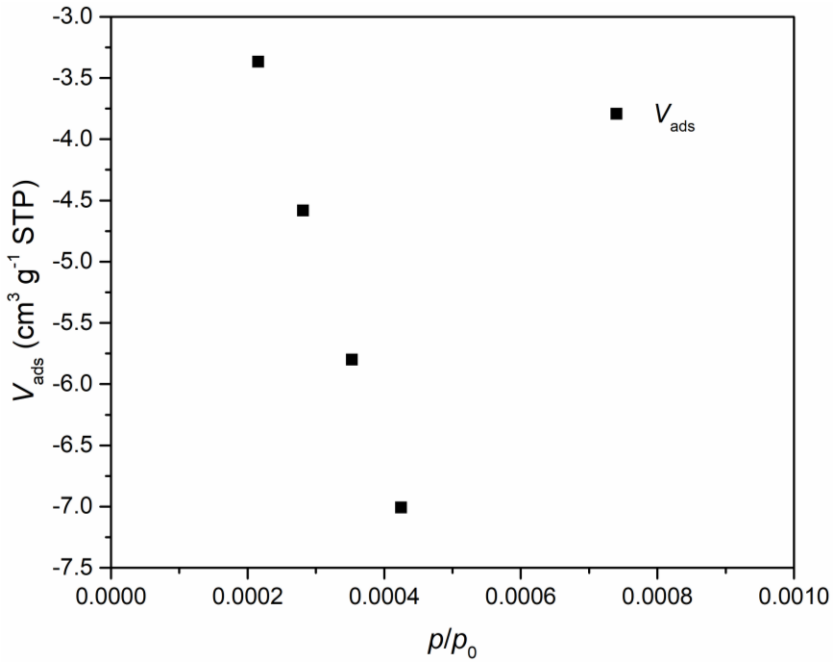

Figure C3. CO_2 adsorption measurement isotherm of PANC-0.2-0.025. Measurement was manually aborted after negative values (corresponding to gas desorption) were noted.

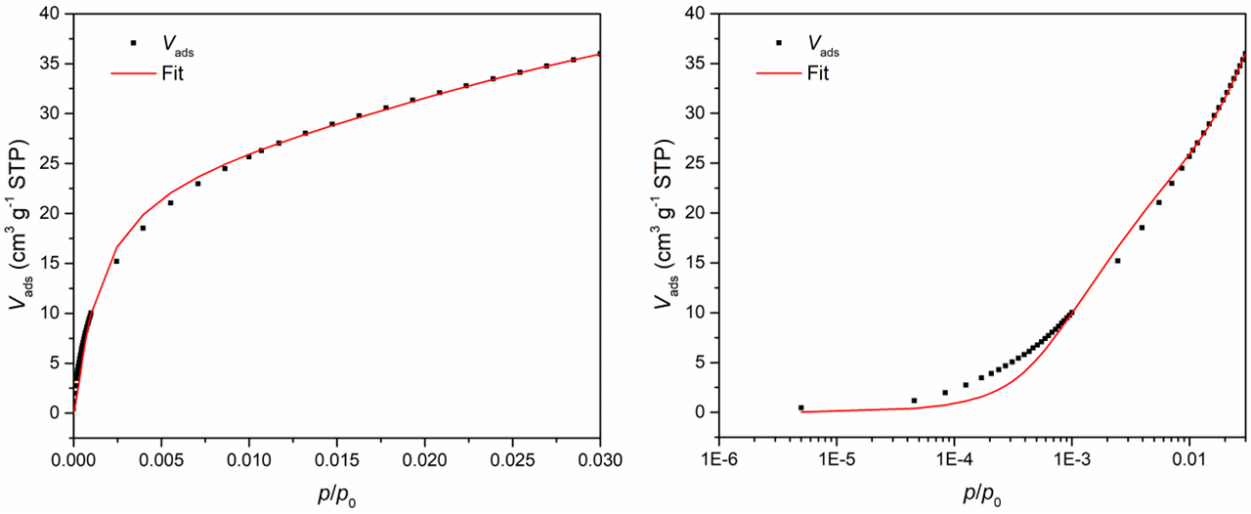

Figure C4. CO_2 adsorption measurement isotherm of PANC-0.1-0.1 along with the fitting curve of 2D-NLDFT-HS model [46] in linear (left) and logarithmic (right) scale on the x-axis. This fit gives a SSA value of 400 m^2 g^{-1}.

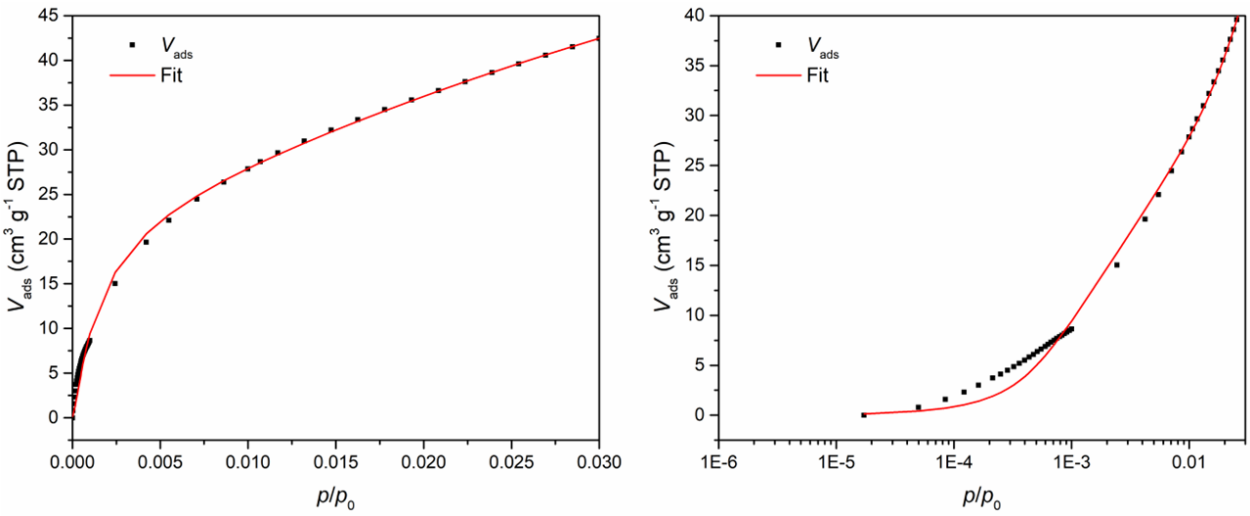

Figure C5. Repeat CO_2 adsorption measurement isotherm of PANC-0.1-0.1 along with the fitting curve of 2D-NLDFT-HS model [46] in linear (left) and logarithmic (right) scale on the x-axis. This fit gives a SSA value of 650 m^2 g^{-1}.

Non-exclusive licence to reproduce the thesis and make the thesis public

I, Egert Möller,

grant the University of Tartu a free permit (non-exclusive licence) to:

reproduce, for the purpose of preservation, including for adding to the DSpace digital archives until the expiry of the term of copyright, my thesis Electrospinning and Subsequent Pyrolysis of $ZnCl_2$-doped Polyacrylonitrile Mats for the Synthesis of Activated Carbon Nanofibers, supervised by Rasmus Palm,

I grant the University of Tartu the permit to make the thesis specified in point 1 available to the public via the web environment of the University of Tartu, including via the DSpace digital archives, under the Creative Commons licence CC BY NC ND 4.0, which allows, by giving appropriate credit to the author, to reproduce, distribute the work and communicate it to the public, and prohibits the creation of derivative works and any commercial use of the work from *06.06.2025* until the expiry of the term of copyright,

I am aware that the author retains the rights specified in points 1 and 2.

4. I confirm that granting the non-exclusive licence does not infringe other persons' intellectual property rights or rights arising from the personal data protection legislation.

Egert Möller

29.05.2023